

1 **Production of protons, deuterons and tritons in**  
2 **argon-nucleus interactions at 3.2 AGeV**

3 BM@N Collaboration

4 **Abstract**

5 Results of the BM@N experiment at the Nuclotron/NICA complex are pre-  
6 sented on proton , deuteron and triton production in interactions of an argon  
7 beam of 3.2 AGeV with fixed targets of C, Al, Cu, Sn and Pb. Transverse  
8 mass distributions, rapidity spectra and multiplicities of protons, deuterons  
9 and tritons are measured. The results are treated within a coalescence ap-  
10 proach and compared with predictions of theoretical models and with other  
11 measurements.

# 1 Introduction

BM@N (Baryonic Matter at Nuclotron) is the first operational experiment at the Nuclotron/NICA accelerator complex. The Nuclotron provides beams of a variety of particles, from proton up to gold ions, with kinetic energy in the range from 1 to 6 GeV/nucleon for light ions with  $Z/A$  ratio of  $\sim 0.5$  and up to 4.5 GeV/nucleon for heavy ions with  $Z/A$  ratio of  $\sim 0.4$ . At these energies, the nucleon density in the fireball created in the collisions of a heavy-ion beam with fixed targets is 3-4 times higher than the nuclear saturation density [1], thus allowing studying heavy-ion interactions in the regime of high-density baryonic matter [2–5].

In the commissioning phase, in a configuration with limited phase-space coverage, BM@N collected first data with beams of carbon, argon, and krypton ions [6, 7]. In the first physics paper BM@N reported on studies of  $\pi^+$  and  $K^+$  production in argon-nucleus interactions [8]. This paper presents results on proton, deuteron and triton production in 3.2 AGeV argon-nucleus interactions.

At these energies, baryon transfer over finite rapidity distances (baryon stopping [9]) plays an important role [10]- [12]. The baryon density, attained in high energy nuclear collisions, is a crucial quantity governing the reaction dynamics and the overall system evolution, including eventual phase transitions. The baryon rapidity distributions in heavy ion collisions for different combinations of projectile and target as well as at different impact parameters provide essential constraints on the dynamical scenarios of baryon stopping. The BM@N experimental arrangement makes it possible to measure the distribution of protons and light nuclei ( $d, t$ ) over the rapidity interval [1.0 - 2.2]. This rapidity range is wide enough to include not only the midrapidity ( $y_{CM} = 1.08$ ), but also the beam rapidity region ( $y_{beam} = 2.16$ ), in contrast to the collider experiments, where the acceptance is usually focused only in the mid-rapidity region. Together with a sufficient  $p_T$ -coverage for nuclear clusters, it is possible at BM@N to better determine the shape of the rapidity density distribution and derive information about rapidity and energy loss in the reaction.

Nuclear cluster production allows one to estimate the nucleon phase-space density attained in the reaction [13]. It governs the overall evolution of the reaction process and may provide information about freeze-out conditions and entropy production in relativistic nucleus-nucleus interactions. A way to measure the nucleon phase-space density is a study of the ratio of deuteron and proton abundances. One of the goals of this work is a study of particle phase-space density evolution in Ar+A collisions for different projectile-target combinations and as a function of collision centrality.

49 In the framework of statistical thermal models, hadron and light nuclei abun-  
50 dances are predicted to be dependent on the bulk parameters of the fireball: the  
51 freeze-out temperature  $T$  and baryochemical potential  $\mu$  [14]. The ratio  $\mu/T$  can  
52 be extracted from the characteristic parameter (penalty factor) describing the mass  
53 dependence of the cluster yield [15]. In this paper, we study the system size and  
54 mass dependence of cluster production to get insight into the thermal parameters  
55 of the particle source.

56 In collisions of heavy nuclei at relativistic energies, a significant fraction of the  
57 initial kinetic energy transforms into particle production and thermal excitation of  
58 matter. Various dynamical models, including those based on hydrodynamics, have  
59 demonstrated that the entropy per baryon,  $S/A$ , created during the initial interac-  
60 tion stage remains constant during the subsequent evolution of the system [16, 17].  
61 Thus, data about entropy production can provide information not only about the  
62 nucleon phase-space density at the final moments of the reaction (freezeout), but  
63 also about the medium properties during the hot and compressed stage. It is also  
64 the aim of this work to study the evolution of the entropy in the reaction zone with  
65 system size in argon-nucleus collisions and compare BM@N results with other  
66 existing experimental data.

67 The binding energies of deuterons and tritons are small compared to freeze-  
68 out temperatures, which are on the order of 100 MeV. These light clusters are  
69 therefore not expected to survive through the high density stages of the collision.  
70 The deuterons and tritons observed in the experiment are formed and emitted at  
71 the end of freeze-out process, and they mainly carry information about this late  
72 stage of the collision.

73 Light cluster production at low energy heavy ion collisions is well described in  
74 a simple coalescence model [18–20] through the distributions of their constituents  
75 (protons and neutrons) and an coalescence parameter  $B_A$  related to the size  $A$   
76 of the cluster. To describe heavy-ion collisions at high energies the simple coales-  
77 cence model is modified taking into account the nucleon phase space distributions  
78 at freeze-out as well as the strength of momentum-space correlations induced by  
79 collective flow [21]. In central heavy-ion collisions the pressure gradient in the  
80 system generates strong transverse radial flow. Therefore nucleon clusters inside a  
81 collective velocity field acquire additional momentum proportional to the cluster’s  
82 mass.

83 The paper is organized as follows. Section 2 describes the experimental set-up  
84 and Section 3 is devoted to details of the event reconstruction. Section 4 describes  
85 the evaluation of the proton, deuteron and triton reconstruction efficiency. Sec-  
86 tion 5 explains the methodology for the definition of centrality classes. Section 6

87 addresses the evaluation of the cross sections, multiplicities and systematic uncer-  
 88 tainties. Transverse mass distributions and rapidity spectra of protons, deuterons  
 89 and tritons are given in Section 7. The BM@N results are compared with pre-  
 90 dictions of the DCM-SMM [22, 23] and PHQMD [24] models. Ratios of the  
 91 transverse momentum distributions of deuterons and tritons to protons are treated  
 92 within a coalescence approach in Section 8. The results are compared with other  
 93 experimental data on nucleus-nucleus interactions. The compound ratios of yields  
 94 of protons and tritons to deuterons are presented in section 10. Finally, a summary  
 95 is given in Section 11.

## 96 2 Experimental set-up

97 The BM@N detector is a forward spectrometer covering the pseudorapidity range  
 98  $1.6 \leq \eta \leq 4.4$ . A schematic view of the BM@N setup in the argon-beam run  
 99 is shown in Fig. 1. More details of all components of the set-up can be found in [25,  
 100 26]. The spectrometer includes a central tracking system consisting of 3 planes of  
 101 forward silicon-strip detectors (ST) and 6 planes of detectors based on gas electron  
 102 multipliers (GEM) [27]. The central tracking system is located downstream of the  
 103 target region inside of a dipole magnet with a bending power of about  $\approx 2.1\text{Tm}$   
 104 and with a gap of 1.05 m between the poles. In the measurements reported here,  
 105 the central tracker covered only the upper half of the magnet acceptance.

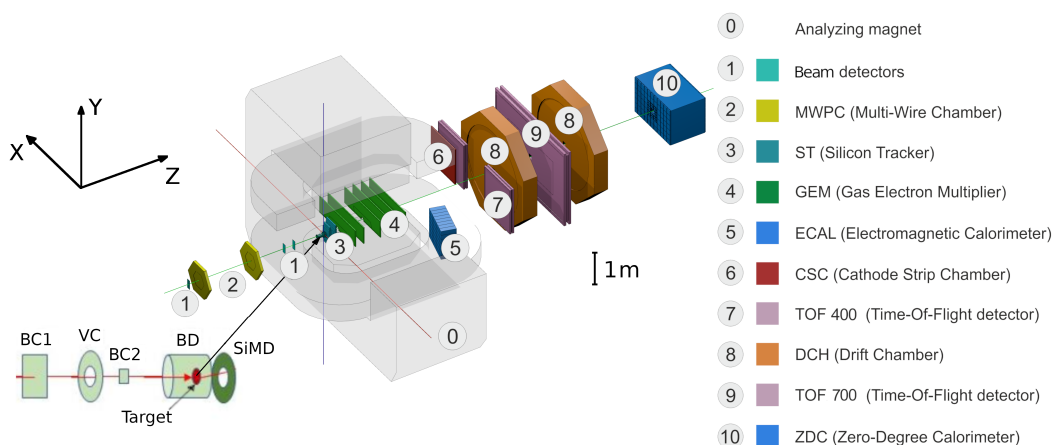


Figure 1: Schematic view of the BM@N setup in the argon beam run.

106 Two sets of drift chambers (DCH), a cathode strip chamber (CSC), two sets

107 of time-of-flight detectors (ToF), and a zero-degree calorimeter (ZDC) are located  
108 downstream of the dipole magnet. The tracking system measures the momentum  
109 of charged particles with a relative uncertainty that varies from 2.5% at a momen-  
110 tum of 0.5 GeV/c to 2% from 1 to 2 GeV/c and rises linearly to 6.5% at 5 GeV/c.  
111 The time resolutions of the ToF-400 [28] and ToF-700 [29] systems are 84 ps and  
112 115 ps, respectively [30].

113 Two beam counters (BC1, BC2), a veto counter (VC), a barrel detector (BD),  
114 and a silicon multiplicity detector (SiMD) are used for event triggering and for  
115 measurement of the incoming beam ions. The BC2 counter provides also the  
116 start time T0 for the time of flight measurement. The BD detector consists of 40  
117 azimuthal scintillating strips arranged around the target, and the SiMD detector  
118 consists of 60 azimuthal silicon segments situated behind the target.

119 To count the number of beam ions that passed through the target, a logical  
120 beam trigger  $BT = BC1 \wedge \overline{VC} \wedge BC2$  was used. The following logic conditions were  
121 applied to generate the trigger signal: 1)  $BT \wedge (BD \geq 3, 4)$ ; 2)  $BT \wedge (SiMD \geq 3, 4)$ ;  
122 3)  $BT \wedge (BD \geq 2) \wedge (SiMD \geq 3)$ . The trigger conditions were varied to find the  
123 optimal ratio between the event rate and the trigger efficiency for each target.  
124 Trigger condition 1 was applied for 60% of the data collected with the carbon  
125 target. This trigger fraction was continuously reduced with the atomic weight  
126 of the target down to 26% for the Pb target. The fraction of data collected with  
127 trigger condition 2 was increased from 6% for the carbon target up to 34% for  
128 the Pb target. The rest of the data were collected with trigger condition 3. Data  
129 were collected with an argon beam intensity of a few  $10^5$  ions per spill and a spill  
130 duration of 2–2.5 sec. The kinetic energy of the beam was 3.2 AGeV with a spread  
131 of about 1%. A set of solid targets of various materials (C, Al, Cu, Sn, Pb) with  
132 a interaction length of 3% was used. The experimental data correspond to a total  
133 integrated luminosity of  $7.8 \mu\text{b}^{-1}$  collected with the different targets:  $2.1 \mu\text{b}^{-1}$   
134 (C),  $2.3 \mu\text{b}^{-1}$  (Al),  $1.8 \mu\text{b}^{-1}$  (Cu),  $1.1 \mu\text{b}^{-1}$  (Sn),  $0.5 \mu\text{b}^{-1}$  (Pb). A total of 16.3M  
135 argon-nucleus collisions at 3.2 AGeV were reconstructed.

### 136 **3 Event reconstruction**

137 Track reconstruction in the central tracker is based on a “cellular automaton” ap-  
138 proach [31] implementing a constrained combinatorial search of track candidates  
139 with their subsequent fitting by a Kalman filter to determine the track parameters.  
140 These tracks are used to reconstruct primary and secondary vertices as well as  
141 global tracks by extrapolation and matching to hits in the downstream detectors

142 (CSC, DCH and ToF).

143 The primary collision vertex position (PV) is measured with a resolution of  
144 2.4 mm in the X-Y plane perpendicular to the beam direction and 3 mm in the  
145 beam direction.

146 Charged particles (protons, deuterons, tritons) are identified using the time of  
147 flight  $\Delta t$  measured between T0 and the ToF detectors, the length of the trajectory  
148  $\Delta l$  and the momentum  $p$  reconstructed in the central tracker. Then the squared  
149 mass  $M^2$  of the particle is calculated by the formula:  $M^2 = p^2((\Delta tc/\Delta l)^2 - 1)$ ,  
150 where  $c$  is the speed of light.

151 The following criteria are required for selecting proton, deuteron and triton  
152 candidates:

- 153 • Each track has at least 4 hits in the GEM detectors (6 detectors in total) [27].  
154 Hits in the forward silicon detectors are used to reconstruct the track, but no  
155 requirements are applied to the number of hits;
- 156 • Tracks originate from the primary vertex. The deviation of the reconstructed  
157 vertex from the nominal target position  $Z_{\text{ver}}$  along the beam direction is  
158 limited to  $-3.4 \text{ cm} < Z_{\text{ver}} - Z_0 < 1.7 \text{ cm}$ . The upper limit corresponds to  
159  $\sim 5.7\sigma$  of the  $Z_{\text{ver}}$  spread and cuts off interactions with the trigger detector  
160 located 3 cm behind the target. The beam interaction rate with the trigger  
161 detector is well below 1% and was not simulated since it does not affect the  
162 precision in Monte Carlo simulation.
- 163 • Distance from the track to the primary vertex in the X-Y plane at  $Z_{\text{ver}}$  (DCA)  
164 is required to be less than 1 cm, which corresponds to  $4\sigma$  of the vertex  
165 resolution in the X-Y plane;
- 166 • Momentum range of positively charged particles is limited by the accep-  
167 tance of the ToF-400 and ToF-700 detectors to  $p > 0.5 \text{ GeV}/c$  and  $p > 0.7$   
168  $\text{GeV}/c$ , respectively;
- 169 • Distance of extrapolated tracks to the CSC (DCH) hits as well as to the ToF-  
170 400 (ToF-700) hits should be within  $\pm 2.5\sigma$  of the momentum dependent  
171 hit-track residual distributions.

172 The mass squared ( $M^2$ ) spectra of positively charged particles produced in  
173 interactions of the 3.2 AGeV argon beam with various targets are shown in Figs. 2a  
174 and 2b for ToF-400 and ToF-700 data, respectively. Particles which satisfy the  
175 above selection criteria contribute to the  $M^2$  spectra. The proton, deuteron and

176 triton signals are extracted in the  $M^2$  windows which depend on rapidity and at  
 177 the maximal rapidity extend from 0.4-1.7  $(\text{GeV}/c^2)^2$ , 2.3-5.0  $(\text{GeV}/c^2)^2$  and 6.6-  
 178 10.0  $(\text{GeV}/c^2)^2$ , respectively. The signals of protons, deuterons and tritons and  
 179 their statistical errors are calculated according to the formulae:  $sig = hist - bg$ ,  
 180  $err_{stat} = \sqrt{hist + bg}$ , assuming the background uncertainty is  $\sqrt{bg}$ . Here  $hist$   
 181 and  $bg$  denote the histogram and background integral yields within the selected  
 182  $M^2$  windows.

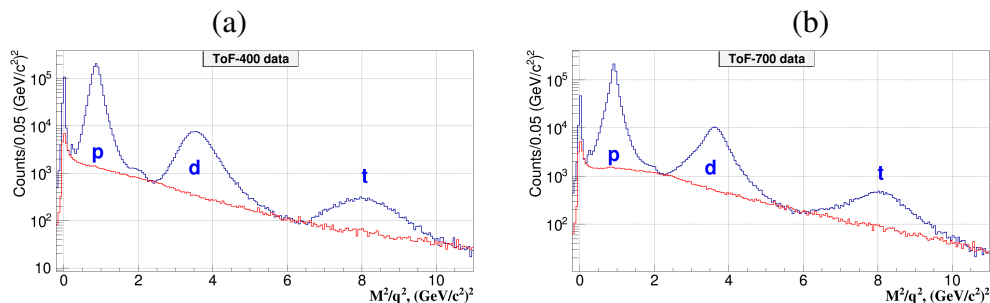


Figure 2:  $M^2$  spectra of positively charged particles produced in argon-nucleus interactions and measured in the ToF-400 (a) and ToF-700 (b) detectors. Peaks of protons, deuterons, tritons are indicated. The red histograms show the background estimated from “mixed events”.

183 The shape of the background under the proton, deuteron and triton signals in  
 184 the  $M^2$  spectra is estimated using the “mixed event” method. For that, tracks re-  
 185 constructed in the central tracker are matched to hits in the ToF detectors taken  
 186 from different events containing a similar number of tracks. The “mixed event”  
 187 background is normalized to the integral of the signal histogram outside the  $M^2$   
 188 windows of protons, deuterons and tritons. It is found that the background level  
 189 differs for light and heavy targets and for different intervals of rapidity and trans-  
 190 verse momentum.

191 The ToF-400 and ToF-700 detectors cover different ranges of rapidity and  
 192 transverse momentum of detected particles. Fig. 3 shows the deuterons measured  
 193 in ToF-400 and ToF-700 in the rapidity vs transverse momentum plane in Ar+Sn  
 194 interactions before making efficiency corrections.

195 The  $dE/dx$  information from the GEM detectors is used to separate the deuteron  
 196 signals from the  $He^4$  signals. The fraction of  $He^4$  in the total  $He^4 + d$  sample is  
 197 calculated in rapidity and transverse momentum bins and subtracted from the data  
 198 signals. The  $He^4$  fraction combined for all the targets is presented in Fig. 4. In  
 199 most of the  $y - p_T$  bins the  $He^4$  fraction does not exceed 3%, only in few bins at  
 200 large  $y$  and low  $p_T$  it reaches 20-35%.

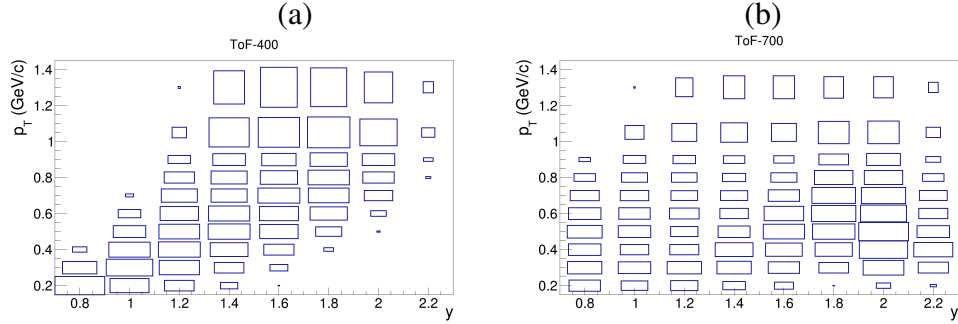


Figure 3: Distribution of the deuteron signals measured in ToF-400 (a) and ToF-700 (b) in the rapidity vs transverse momentum plane in Ar+Sn interactions.

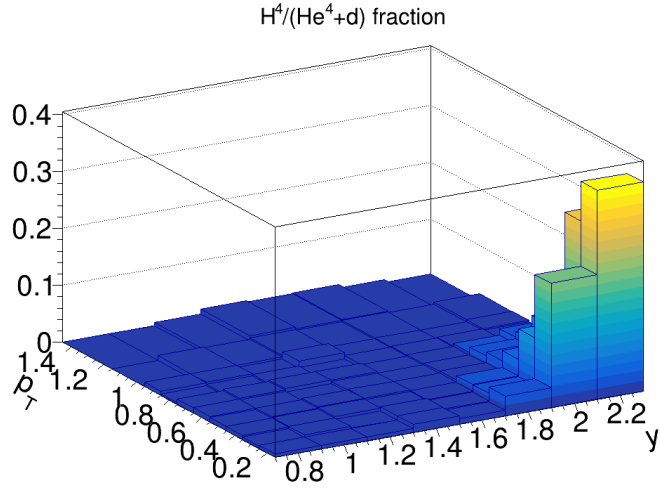


Figure 4: Fraction of  $He^4$  in the  $He^4 + d$  sample measured in the rapidity vs transverse momentum plane in Ar+A interactions.

## 201 **4 Reconstruction efficiency and trigger performance**

202 To evaluate the proton, deuteron and triton reconstruction efficiency, Monte Carlo  
 203 data samples of argon-nucleus collisions were produced with the DCM-SMM  
 204 event generator [22, 23]. Propagation of particles through the entire detector  
 205 volume and responses of the detectors were simulated using the GEANT3 pro-  
 206 gram [32] integrated into the BmnRoot software framework [33].

207 The efficiencies of the silicon, GEM, CSC, DCH and ToF detectors were ad-  
 208 justed in the simulation in accordance with the measured detector efficiencies [34].  
 209 The Monte Carlo events went through the same chain of reconstruction and iden-  
 210 tification as the experimental events. More details of the simulation are given in



211 ref. [8].

212 The proton, deuteron and triton reconstruction efficiencies are calculated in  
 213 intervals of rapidity  $y$  and transverse momentum  $p_T$ . The reconstruction efficiency  
 214 includes the geometrical acceptance, the detector efficiency, the kinematic and  
 215 spatial cuts, the loss of protons, deuterons and tritons due to in-flight interactions.  
 216 The reconstruction efficiencies of protons and deuterons detected in ToF-400 and  
 217 ToF-700 are shown in Fig. 5 as functions of  $y$  (upper panel) and  $p_T$  (lower panel)  
 218 for Ar+Sn interactions.

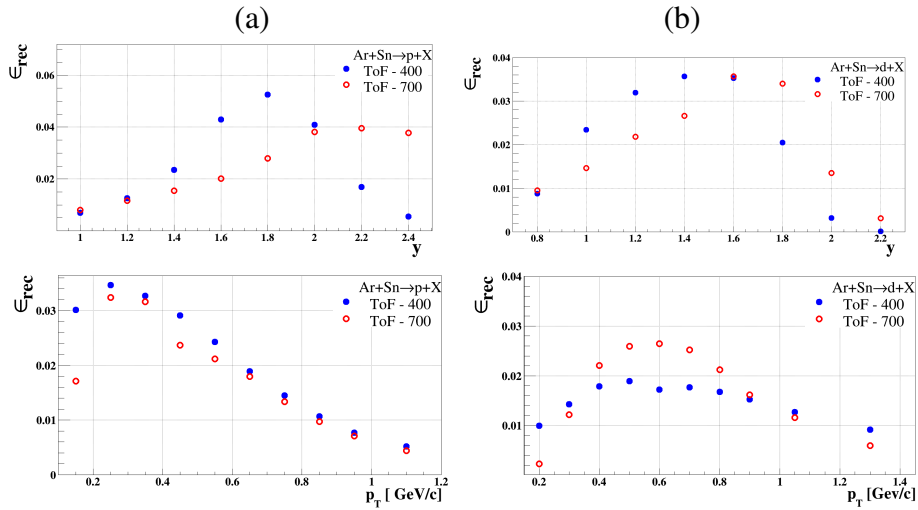


Figure 5: Reconstruction efficiency of protons (a) and deuterons (b) produced in Ar+Sn collisions, detected in ToF-400 (full blue circles) and ToF-700 (open red circles) as functions of rapidity  $y$  and  $p_T$ . The efficiency includes both acceptance and reconstruction.

219 The trigger efficiency  $\epsilon_{trig}$  depends on the number of fired channels in the BD  
 220 (SiMD) detectors. It was calculated for events with reconstructed protons, deuterons and  
 221 tritons using event samples recorded with an independent trigger based on  
 222 the SiMD (BD) detectors. The BD and SiMD detectors cover different and non-  
 223 overlapping regions of the BM@N acceptance, that is, they detect different collision  
 224 products. The efficiency of the combined BD and SiMD triggers was calculated as the  
 225 product of the efficiencies of the BD and SiMD triggers. The trigger efficiency  
 226 decreases with a decrease in the mass of the target and an increase in the  
 227 centrality of the collision. More details of the trigger efficiencies evaluation  
 228 are given in ref. [8].

## 5 Centrality classes

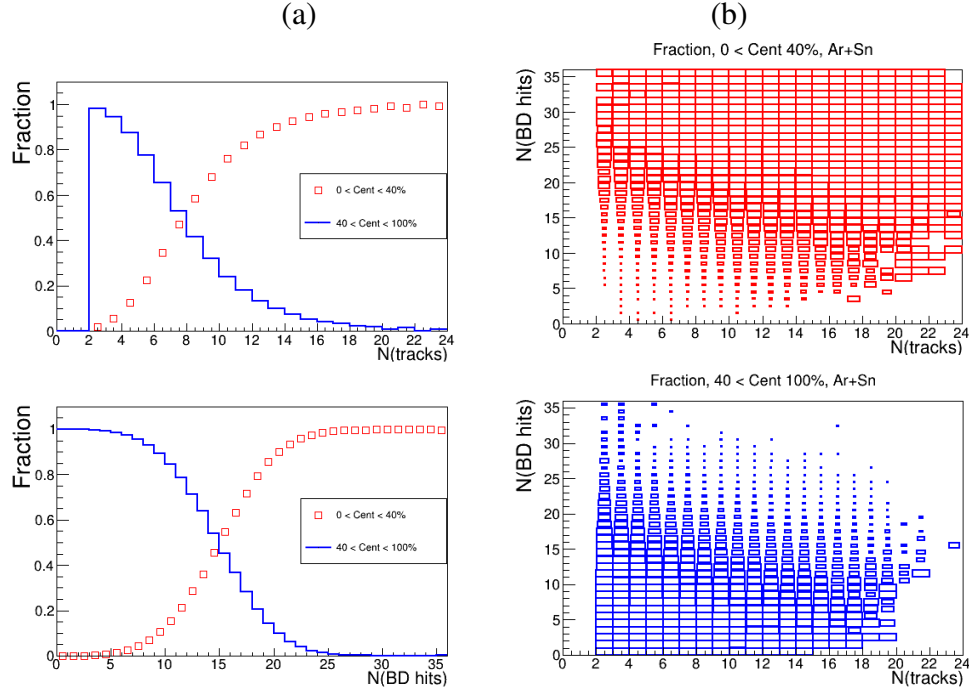


Figure 6: (a) Fraction (probability) of events with centrality 0-40% (red open symbols) and 40-100% (blue histogram) as a function of the number of tracks  $N(\text{tracks})$  in the primary vertex (upper plot) and the number of hits  $N(\text{BD})$  in the BD detector (lower plot). (b) two-dimensional distribution of the fraction (probability) of events with centrality 0-40% (upper red histogram) and 40-100% (lower blue histogram) as a function of  $N(\text{tracks})$  (horizontal axis) and  $N(\text{BD})$  (vertical axis).

230 The event centrality is determined as the fraction of the interaction cross section  
 231 in the interval  $[0, b]$  of the impact parameter  $b$  of the nucleus-nucleus collision  
 232 to the total inelastic interaction cross section. Two classes of centrality: 1) 0-40%  
 233 of the cross section (more central collisions) and 2) 40-100% of the cross section  
 234 ( more peripheral collisions), are defined from the impact parameter distributions  
 235 of Ar+A inelastic interactions simulated by the DCM-SMM model. The boundary  
 236 impact parameter  $b_{cut}$  for the definition of the two classes for interactions of Ar  
 237 with various targets is given in Table 2. It was found that the number of tracks  
 238 originated from the primary event vertex  $N(\text{tracks})$  and the number of hits in the  
 239 Barrel Detector  $N(\text{BD})$  are anti-correlated with the impact parameter  $b$ . Using

240 results of the DCM-SMM Monte Carlo simulation, the fractions of reconstructed  
 241 events, which belong to the centrality classes 0-40% and 40-100%, are calculated.  
 242 Fractions of events with centrality 0-40% and 40-100% are presented in Fig. 6 as  
 243 functions of  $N(\text{tracks})$ ,  $N(\text{BD})$  and as a two-dimensional distribution  $N(\text{tracks}) /$   
 244  $N(\text{BD})$ .

245 Fractions (probabilities) of events with centrality 0-40% and 40-100%, taken  
 246 from the two-dimensional  $N(\text{tracks}) / N(\text{BD})$  distributions are used as event weights  
 247 to define the weighted number of reconstructed protons, deuterons and tritons in  
 248 the  $y$  and  $p_T$  bins in data and simulation. The systematic uncertainty of the event  
 249 centrality is estimated from the remaining difference in the shape of the  $N(\text{tracks})$   
 250 and  $N(\text{BD})$  distributions in  $y$  and  $p_T$  bins in the simulation relative to the data.

## 251 **6 Cross sections, multiplicities, and systematic un-** 252 **certainties**

253 The protons, deuterons and tritons in Ar+C, Al, Cu, Sn, Pb interactions are mea-  
 254 sured in the following kinematic ranges: transverse momentum  $0.1 < p_T <$   
 255  $1.2 \text{ GeV}/c$  (protons),  $0.15 < p_T < 1.45 \text{ GeV}/c$  (deuterons),  $0.2 < p_T < 1.6 \text{ GeV}/c$   
 256 (tritons) and rapidity in the laboratory frame  $0.9 < y < 2.5$  (protons),  $0.7 <$   
 257  $y < 2.3$  (deuterons),  $0.7 < y < 2.1$  (tritons). The differential cross sections  
 258  $d^2\sigma_{p,d,t}(y, p_T)/dydp_T$  and multiplicities  $d^2N_{p,d,t}(y, p_T)/dydp_T$  of protons, deuterons  
 259 and tritons produced in Ar+C, Al, Cu, Sn, Pb interactions are calculated using the  
 260 relations:

$$261 \quad d^2\sigma_{p,d,t}(y, p_T)/dydp_T = \Sigma[d^2n_{p,d,t}(y, p_T, N_{tr})/(\epsilon_{trig}(N_{tr})dydp_T)] \times 1/(L\epsilon_{p,d,t}^{rec}(y, p_T))$$

$$d^2N_{p,d,t}(y, p_T)/dydp_T = d^2\sigma_{p,d,t}(y, p_T)/(\sigma_{inel}dydp_T) \quad (1)$$

262 where the sum is performed over bins of the number of tracks in the primary  
 263 vertex,  $N_{tr}$ ,  $n_{p,d,t}(y, p_T, N_{tr})$  is the number of reconstructed protons, deuterons  
 264 and tritons in the intervals  $dy$  and  $dp_T$ ,  $\epsilon_{trig}(N_{tr})$  is the track-dependent trigger  
 265 efficiency,  $\epsilon_{p,d,t}^{rec}(y, p_T)$  is the reconstruction efficiency of protons, deuterons and  
 266 tritons,  $L$  is the luminosity and  $\sigma_{inel}$  is the inelastic cross section for argon-nucleus  
 267 interactions. The cross sections and multiplicities are evaluated for the two cen-  
 268 trality classes: 0-40% and 40-100%.

269 Several sources are considered for the evaluation of the systematic uncertainty  
 270 of the proton, deuteron and triton yield,  $n_{p,d,t}$ , and the reconstruction efficiency  
 271  $\epsilon_{rec}$ . Some of them affect both the yield  $n_{p,d,t}$  and the reconstruction efficiency,

Table 1: Mean systematic uncertainties averaged over the  $y, p_T$  ranges of protons, deuterons and tritons measured in argon-nucleus interactions.

	Ar+C %	Ar+Al %	Ar+Cu %	Ar+Sn %	Ar+Pb %
$\epsilon_{trig}$ p,d,t	9	7	7	7	7
<b>protons</b>					
$n_p, \epsilon_{rec}$	15	6	8	14	11
<b>Total</b>	18	9	11	16	13
<b>deuterons</b>					
$n_d, \epsilon_{rec}$	32	22	20	19	22
<b>Total</b>	33	23	21	20	23
<b>tritons</b>					
$n_t, \epsilon_{rec}$	43	22	20	20	22
<b>Total</b>	44	23	21	21	23

Table 2: The boundary impact parameter  $b_{cut}$  for definition of two classes of centrality, 0-40% and 40-100%, in inelastic Ar+A interactions. The inclusive cross section  $\sigma_{inel}$  for inelastic Ar+A interactions.

	Ar+C	Ar+Al	Ar+Cu	Ar+Sn	Ar+Pb
$b_{cut}$ , fm	4.23	4.86	5.66	6.32	7.10
$\sigma_{inel}$ , mb [35]	$1470 \pm 50$	$1860 \pm 50$	$2480 \pm 50$	$3140 \pm 50$	$3940 \pm 50$

272  $\epsilon_{rec}$ . For these cases the correlated effect is taken into account by considering  
 273 the variations on the  $n_{p,d,t}/\epsilon_{rec}$  ratio: A detailed consideration of the systematic  
 274 uncertainties is done in ref. [8]. Sources specific for this analysis are listed below:

- 275 • Systematic uncertainty of the background subtraction in the mass-squared  
 276  $M^2$  spectra of identified particles: it is estimated as the difference between  
 277 the background integral under the  $p, d, t$  mass-squared windows taken from  
 278 “mixed events” (as described in Section 3) and from the fitting of the  $M^2$   
 279 spectra by a linear function. The latter is done in the  $M^2$  range, excluding  
 280 the proton, deuteron and triton signal windows.
- 281 • Systematic uncertainty calculated as half of the difference between the p/d/t  
 282 yield measured in the ToF-400 and ToF-700 detectors in bins of rapidity  $y$ .
- 283 • Systematic uncertainty of the event centrality weights estimated 1) from the  
 284 remaining difference in the shape of the N(track) and N(BD) distributions  
 285 in  $y$  and  $p_T$  bins in the data and the simulation; 2) from the difference in the  
 286 event centrality weights taken from the two-dimensional N(track) / N(BD)  
 287 distribution relative to the one-dimensional N(BD) distribution.

288 Table 1 summarizes the mean values, averaged over  $p_T, y$  and  $N_{tr}$  of the system-  
 289 atic uncertainties of the various factors of Eq. (1),  $n_{p,d,t}, \epsilon_{rec}$ , and  $\epsilon_{trig}$ . The total  
 290 systematic uncertainty of the yield and reconstruction efficiency for the various  
 291 targets is calculated as a square sum of uncertainties from different sources.

292 The luminosity is calculated from the beam flux  $\Phi$  as given by the beam trigger  
 293 (see Section 2) and the target thickness  $l$  using the relation:  $L = \Phi\rho l$  where  $\rho$   
 294 is the target density expressed in atoms/cm<sup>3</sup>. The systematic uncertainty of the  
 295 luminosity is estimated from the fraction of the beam which can miss the target,  
 296 determined from the vertex positions, and found to be within 2%.

297 A detailed discussion of the systematic uncertainty of the trigger efficiency is  
 298 given in ref. [8]. The total systematic uncertainty of the trigger efficiency for the  
 299 various targets is listed in Table 1.

300 The inelastic cross sections of Ar+C, Al, Cu, Sn, Pb interactions are taken  
 301 from the predictions of the DCM-SMM model. The  $\sigma_{inel}$  uncertainties for Ar+C,  
 302 Al, Cu, Sn, Pb interactions are estimated from the empirical formulas taken from  
 303 ref. [35, 36] and given in Table 2.

## 304 7 Rapidity and mean transverse mass spectra

305 At a kinetic energy of 3.2 GeV/nucleon, the rapidity of the nucleon-nucleon center-  
 306 of-mass (CM) system is  $y_{CM} = 1.08$ . The rapidity intervals covered in the present

307 measurements,  $0.9 < y < 2.5$ ,  $0.7 < y < 2.3$  and  $0.7 < y < 2.1$  for protons,  
 308 deuterons and tritons, respectively, correspond therefore to the forward and central  
 309 rapidity regions in the nucleon-nucleon CM system. The yields of protons,  
 310 deuterons and tritons measured in the  $m_T$  and  $y$  bins in the two centrality inter-  
 311 vals in Ar+C,Al,Cu,Sn,Pb interactions can be found in ref. [37].

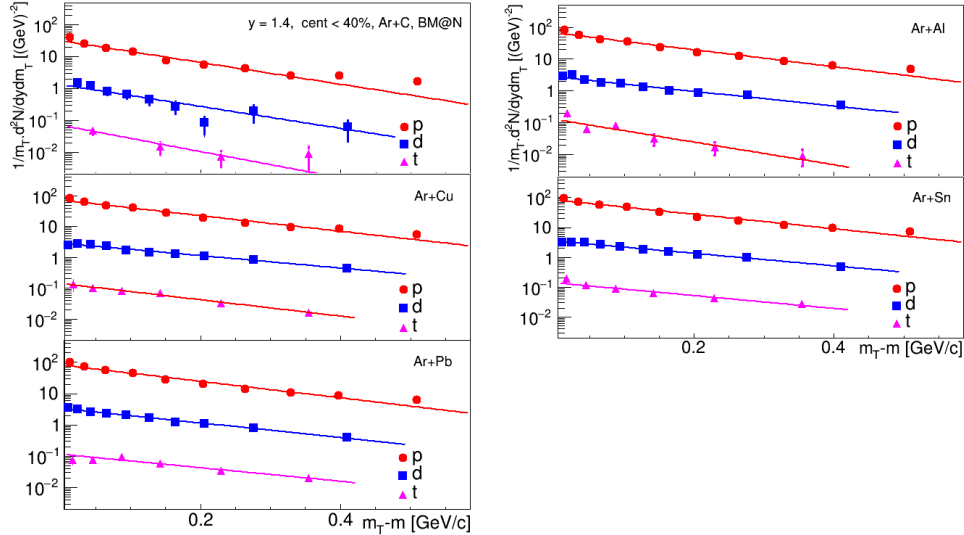


Figure 7: Transverse mass spectra of protons, deuterons, tritons produced at rapidity  $y = 1.4$  in Ar+C, Al, Cu, Sn, Pb interactions with centrality 0-40%. The vertical bars and boxes represent the statistical and systematic uncertainties, respectively. The lines show the results of the fit by an exponential function.

312 The transverse mass  $m_T = \sqrt{m_{p,d,t}^2 + p_T^2}$  spectra of protons, deuterons and  
 313 tritons produced in various targets at  $y = 1.4$  in the 0-40% centrality class are  
 314 shown in Figs. 7. The spectra are parameterised by an exponential function as:

$$1/m_T \cdot d^2N/dy dm_T = \frac{dN/dy}{T_0(T_0 + m)} \cdot \exp(-(m_T - m)/T_0) \quad (2)$$

315 where fitting parameters are the integral of the  $m_T$  spectrum,  $dN/dy$ , and the  
 316 inverse slope,  $T_0$ . The  $dN/dy$  values integrated over the entire  $p_T$  range and the  $T_0$   
 317 values are extracted from the fit. They can be found in ref. [37]. The  $T_0$  values are  
 318 used to calculate the mean transverse kinetic energy  $\langle E_T \rangle$  according to equation  
 319 3. The  $dN/dy$  spectra of protons, deuterons and tritons produced in collisions  
 320 with centrality 0-40% in the various targets are shown in Figs. 8a, 9a and 10a,  
 321 respectively.

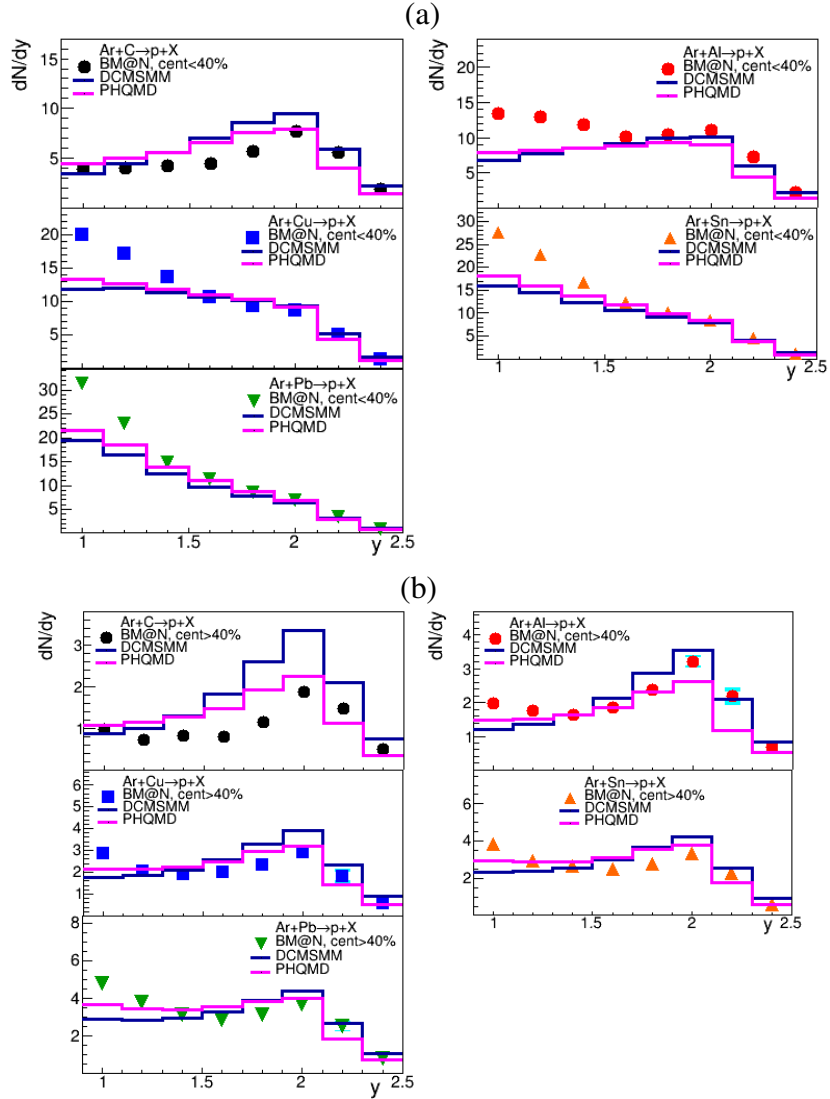


Figure 8: Rapidity spectra  $dN/dy$  of protons produced in Ar+C, Al, Cu, Sn, Pb interactions with centrality 0-40% (a) and 40-100% (b). The results are integrated over  $p_T$ . The vertical bars and boxes represent the statistical and systematic uncertainties, respectively. The predictions of the DCM-SMM and PHQMD models are shown as blue and magenta lines.

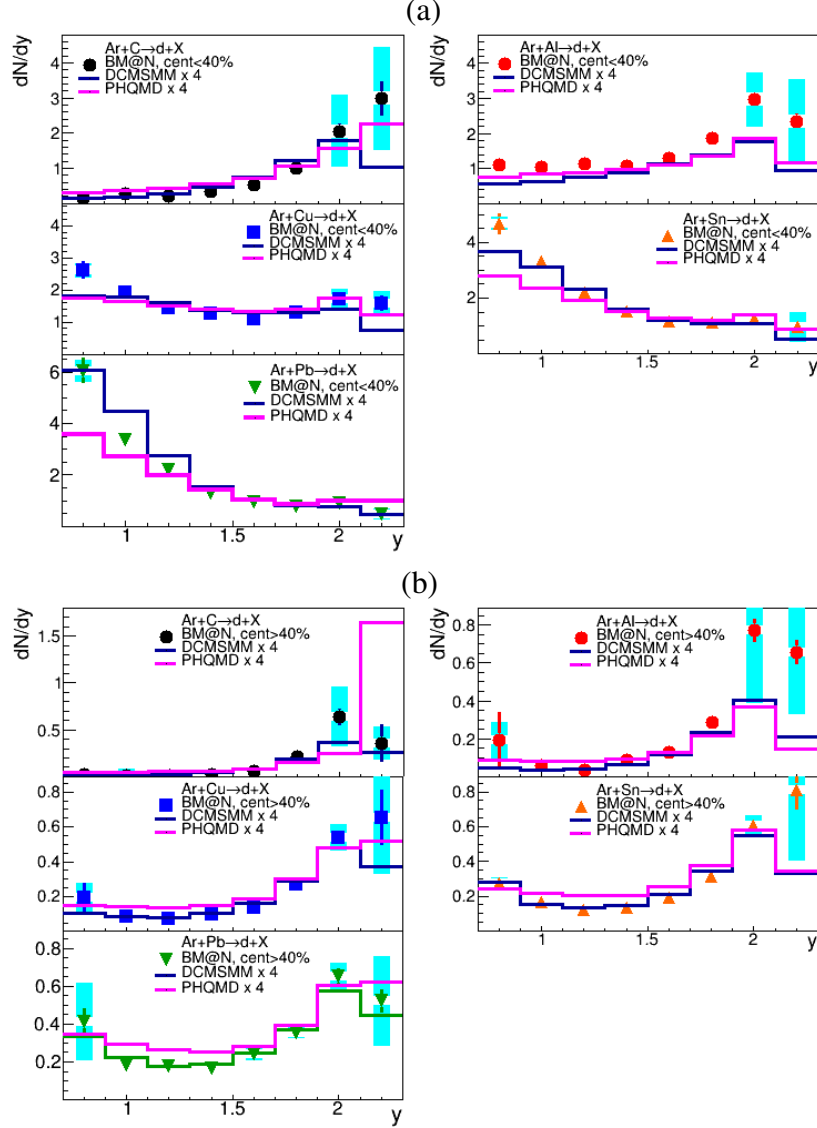


Figure 9: Rapidity spectra  $dN/dy$  of deuterons produced in Ar+C, Al, Cu, Sn, Pb interactions with centrality 0-40% (a) and 40-100% (b). The results are integrated over  $p_T$ . The vertical bars and boxes represent the statistical and systematic uncertainties, respectively. The predictions of the DCM-SMM and PHQMD models, multiplied by a factor 4, are shown as blue and magenta lines.



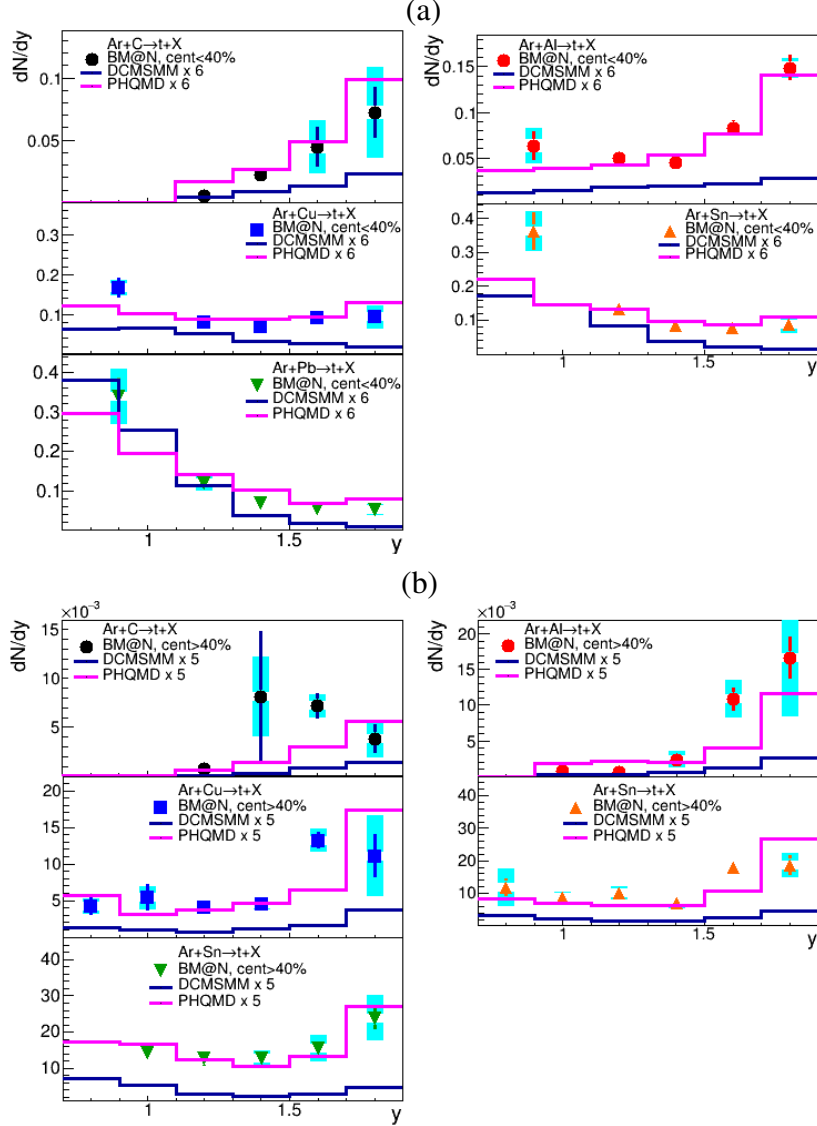


Figure 10: Rapidity spectra  $dN/dy$  of tritons produced in Ar+C,Al, Cu, Sn, Pb interactions with centrality 0-40% (a) and 40-100% (b). The results are integrated over  $p_T$ . The vertical bars and boxes represent the statistical and systematic uncertainties, respectively. The predictions of the DCM-SMM and PQHMD models, multiplied by factors 6 in (a) and 5 in (b), are shown as blue and magenta lines.

322 It is seen that the particle rapidity spectral shapes vary strongly with the tar-  
 323 get mass. The experimental results are compared with predictions of the DCM-  
 324 SMM [22, 23] and PHQMD [24] models. For protons, the models have quite  
 325 similar predictions, which are in reasonable agreement with the experimental re-  
 326 sults in the forward rapidity range. At mid-rapidity the models under-estimate the  
 327 data for interactions with the targets heavier than the carbon, this might indicate  
 328 that the degree of nuclear stopping in the data is higher than in the models.

329 Deuterons and tritons are predominately produced in the beam fragmenta-  
 330 tion region for Ar+C and Ar+Al interactions, whereas for heavier targets they  
 331 are mostly produced at mid-rapidity. For deuterons and tritons, the models rea-  
 332 sonably describe the shape of the experimental spectra, but under-predict the ab-  
 333 solute yields by factors of 4 and 6, respectively. The  $dN/dy$  spectra of protons,  
 334 deuterons and tritons produced in collisions with centrality 40-100% in the various  
 335 targets are shown in Figs. 8b, 9b and 10b, respectively. The largest contribution  
 336 is observed in the beam fragmentation range for all the targets. This tendency  
 337 is reproduced by the DCM-SMM and PHQMD models, but here also the mod-  
 338 els under-estimate the absolute yields for deuterons and tritons by factors 4 and  
 339 5, respectively. A similar effect has been reported by the STAR experiment. A  
 340 significant deficit of deuterons and tritons in the PHQMD model relative to the  
 341 experimental data has been observed in central (0-10%) collisions of Au+Au at  
 342  $\sqrt{s}$  of 3 GeV [38].

343 The observed discrepancy between the data and the DCM-SMM and PHQMD  
 344 models could be due to feed-down from excited nuclear states that is not taken into  
 345 account in the models. At BM@N collision energies, the reaction zone consists of  
 346 a hadronic gas which is dominated by nucleons and stable nuclei ( $d, t, {}^3\text{He}, {}^4\text{He}$ ).  
 347 However, in addition to these, there are many excited nuclear states with mass  
 348 number  $A \geq 4$ . The role of the feeddown from these states for the description  
 349 of light nuclei production in a broad energy range was discussed in ref. [39]. A  
 350 quantitative estimate of the feed-down contributions to deuterons and tritons was  
 351 performed in the framework of a hadron resonance gas model, supplemented by  
 352 a list of  $A=4$  and  $A=5$  excited nuclear states from [40]. As reported in [39],  
 353 feeding gives a significant contribution to the yields of  $d, t$  at NICA/BM@N en-  
 354 ergies: as much as 60% of all final tritons and 20% of deuterons may come from  
 355 the decays of excited nuclear states.

356 The mean transverse kinetic energy, defined as  $\langle E_T \rangle = \langle m_T \rangle - m$ , is related to  
 357 the  $T_0$  value extracted from the fit of the  $m_T$  spectrum by the following equation:

$$\langle E_T \rangle = \langle m_T \rangle - m = T_0 + T_0^2 / (T_0 + m) \quad (3)$$

358 The  $\langle E_T \rangle$  values obtained from the fits of the proton spectra in the 0-40% cen-  
 359 trality class are shown in Fig. 11a as a function of rapidity. The maximal values  
 360 of  $\langle E_T \rangle$  are measured at rapidity  $1.0 < y < 1.3$ , i.e. at mid-rapidity in the CM  
 361 system. In general, the  $y$  dependence of  $\langle E_T \rangle$  for protons is consistent with pre-  
 362 dictions of the DCM-SMM and PHQMD models.

363 The  $\langle E_T \rangle$  values for deuterons and tritons in the 0-40% centrality class are  
 364 shown as a function of rapidity in Figs. 11b and 11c, respectively. PHQMD  
 365 reproduces the rise of the data at mid-rapidity in CM for deuterons and tritons  
 366 relative to protons, where as the DCM-SMM model predicts similar  $\langle E_T \rangle$  values  
 367 for protons, deuterons and tritons in contradiction with the experimental results.

368 The mid-rapidity value  $\langle E_T(y^* = 0) \rangle$  is calculated as the average over the  
 369 three points at  $y=1.0, 1.2$  and  $1.4$ . To cross-check the result of this averaging, the  
 370 rapidity dependence of  $\langle E_T \rangle$  for each particle sort in Fig. 11 was fitted with a func-  
 371 tional form  $E_T(0)/\cosh y^*$  with the midrapidity transverse energy  $E_T(0)$  being  
 372 the fit parameter. We found that the difference between  $E_T(0)$  and  $\langle E_T(y^* = 0) \rangle$   
 373 is less than 2% and it was disregarded. Figure 12 shows the dependence of the  
 374 mid-rapidity values of  $\langle E_T \rangle$  on the mass of the nuclear fragment. It is seen, that  
 375  $\langle E_T \rangle$  rises approximately linearly with the mass of the nuclear fragment. For the  
 376 Ar+C colliding system no mass dependence of the  $\langle E_T \rangle$  value is observed.

377 The mean transverse kinetic energy could be expressed as the sum of the en-  
 378 ergy of radial flow and random thermal motion as [41]:

$$\langle E_T \rangle \approx E_{therm} + E_{flow} = 3/2T^* + (\gamma - 1)m \quad (4)$$

379 where  $\gamma = 1/\sqrt{1 - \langle \beta \rangle^2}$ ,  $\langle \beta \rangle$  is the average radial collective velocity and  $T^*$   
 380 is the temperature of the thermal motion and  $m$  is the fragment mass. The pa-  
 381 rameter  $T^*$ , that can be obtained from the extrapolation of the linear fits to zero  
 382 mass, cannot be directly related to the source temperature since the temperature  
 383 in expanding fireballs is blue shifted as:

$$T^* = T \sqrt{(1 + \langle \beta \rangle)/(1 - \langle \beta \rangle)} \quad (5)$$

384 Thus, in order to obtain the true temperature, the  $T^*$  parameter is corrected by  
 385 the blue-shift factor according to equation 5. The average radial velocity  $\langle \beta \rangle$  and  
 386 source temperature at the kinetic freeze-out extracted from these fits are given in  
 387 Table 3. One finds a flow velocity consistent with zero in central Ar+C collisions.  
 388 Nuclear collisions of such small systems can be considered as a superposition  
 389 of the independent nucleon-nucleon interactions, therefore, the density of partic-  
 390 ipants that has been reached in these reactions is probably not high enough to

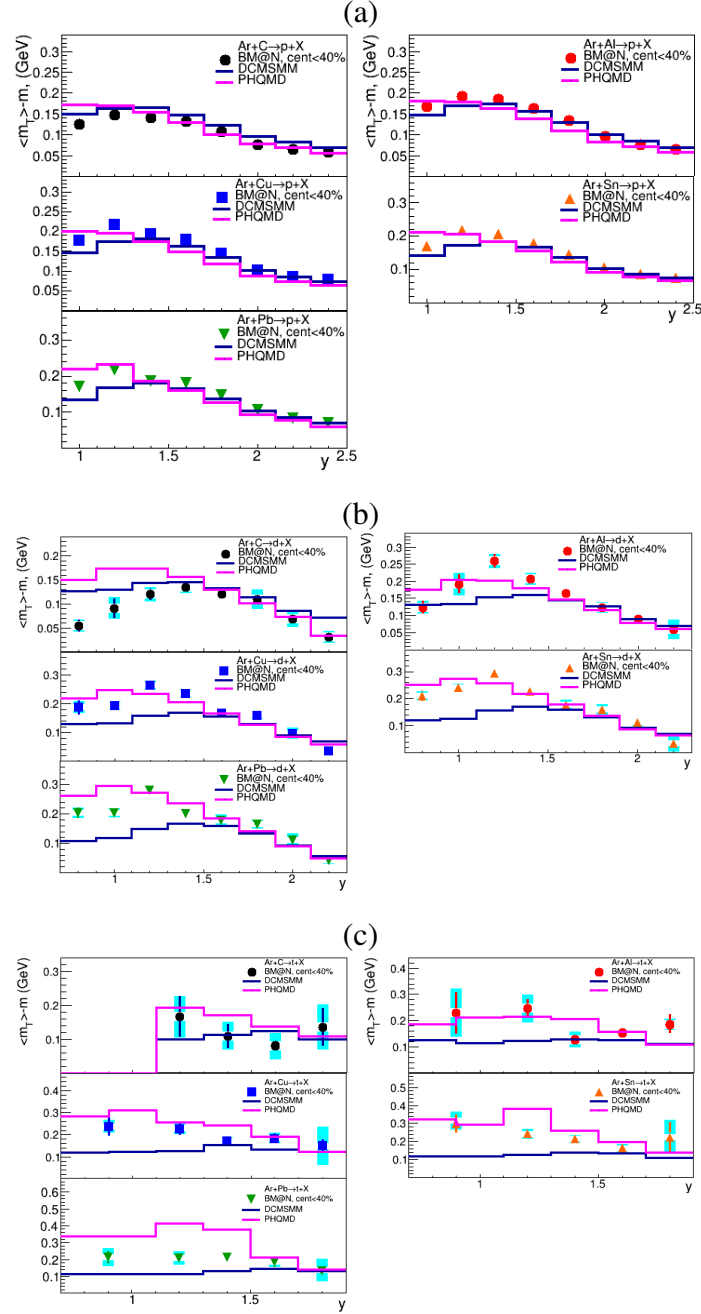


Figure 11: Rapidity  $y$  dependence of the mean transverse kinetic energy  $\langle m_T \rangle - m$  determined from the fits of the  $m_T$  spectra of protons (a), deuterons (b) and tritons (c) in Ar+C, Al, Cu, Sn, Pb interactions with centrality 0-40%. The vertical bars and boxes represent the statistical and systematic uncertainties, respectively. The predictions of the DCM-SMM and PHQMD models are shown as blue and magenta lines.

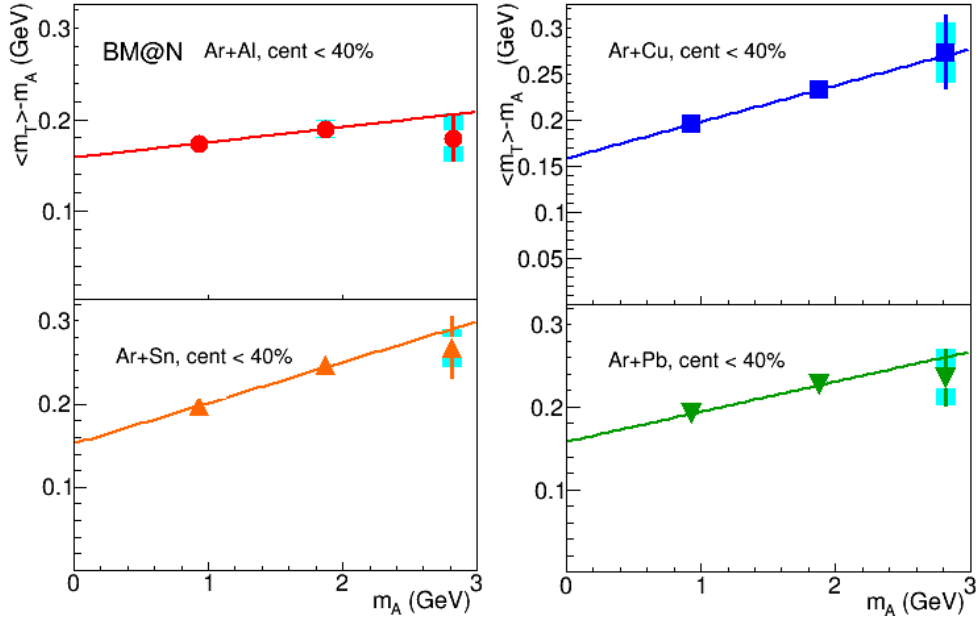


Figure 12: Dependence of the mean transverse kinetic energy  $\langle m_T \rangle - m$  on the mass of the nuclear fragment measured in Ar+Al,Cu,Sn,Pb collisions with centrality 0-40%. Linear fits to the data points are indicated by dashed lines.

391 create a fireball with strong collective behavior. In contrast, for larger colliding  
 392 systems (Ar+Al,Cu,Sn,Pb) the particle density and the re-scattering rate inside  
 393 the reaction zone are higher, giving rise to the mean expansion velocity. It appears  
 394 that the observed mass dependence for  $T$  and  $\langle \beta \rangle$  is weak at BM@N energies: the  
 395 fits give nearly the same temperature and a slight increase of the flow velocity. It  
 396 might be an indication that the increase of the reaction volume and the number  
 397 of collisions with the target mass does not accompanied by a significant compression  
 398 of nuclear matter (note also discussion about the degree of nuclear stopping  
 399 in Section 9).

400 The BM@N radial flow results could be compared with measurements at  
 401 lower and higher energies. The FOPI experiment measured  $\langle \beta \rangle \sim 0.35$  in Au+Au  
 402 collisions at 1.2 AGeV and found that the radial flow decreases below  $\langle \beta \rangle \sim 0.20$   
 403 at even lower energies and in interactions of middle-size nuclei compared to heavy  
 404 nuclei [42]. Measurements of the EOS experiment [43] in Au+Au collisions  
 405 are consistent with these results. At higher energies the NA49 [41] and STAR  
 406 BES [44, 45] experiments measured  $\langle \beta \rangle \sim 0.45$  in interactions of heavy nuclei  
 407 (Pb+Pb and Au+Au). The STAR experiment measured that the  $\langle \beta \rangle$  values de-  
 408 crease with decreasing of the colliding system size [45]. The experiments also  
 409 found that the temperature  $T$  increases from  $\sim 30$  MeV to  $\sim 120$  MeV from en-

410 ergies of FOPI to NA-49 and STAR BES. The  $\langle\beta\rangle$  and  $T$  values measured by  
 411 BM@N in argon-nucleus interactions (except for Ar+C) lay between the values  
 412 measured with heavy nuclei at lower and higher energies taking into account also  
 a reduced size of the Ar+A system.

Table 3:  $T$  and  $\langle\beta\rangle$  values evaluated from the linear fit of the  $\langle E_T \rangle = \langle m_T \rangle - m$  values of protons, deuterons and tritons produced in Ar+A interactions with centrality 0-40%.

	Ar+C	Ar+Al	Ar+Cu	Ar+Sn	Ar+Pb
T, MeV	$89 \pm 3$	$91 \pm 5$	$80 \pm 5$	$76 \pm 5$	$80 \pm 5$
$\langle\beta\rangle$	$0.0 \pm 0.05$	$0.17 \pm 0.05$	$0.27 \pm 0.03$	$0.30 \pm 0.03$	$0.26 \pm 0.03$

413

## 414 8 Coalescence factors

415 Within a coalescence model [18, 19] nuclear fragment formation is characterized  
 416 by a coalescence factor  $B_A$ , defined through the invariant momentum spectra by  
 417 the equation:

$$418 \quad E_A d^3 N_A / d^3 p_A = B_A (E_p d^3 N_p / d^3 p)^Z (E_n d^3 N_n / d^3 p)_{p=p_A/A}^{A-Z}$$

419 where  $p_A$  and  $p = p_A/A$  are momenta of the nuclear fragment A and the nucleon,  
 420 respectively. It relates the yield  $N_A$  of nuclear fragments with charge  $Z$  and atomic  
 421 mass number  $A$  to the yields of the coalescing nucleons  $N_p$  and  $N_n$  at the same  
 422 velocity. Assuming that the neutron momentum density is equal to the proton  
 423 momentum density at freeze-out, the  $B_A$  value can be calculated as:

$$B_A = d^2 N_A / 2\pi p_{T,A} d p_{T,A} dy / (d^2 N_p / 2\pi p_T d p_T dy)^A \quad (6)$$

424 In a thermodynamic approach [46, 47]  $B_A$  is inversely related to the fireball vol-  
 425 ume:  $B_A \sim V_{eff}^{1-A}$ . In accordance with model expectations [21] strong position-  
 426 momentum correlations present in the expanding source lead to a higher coales-  
 427 cence probability at larger values of  $p_T$ . Assuming a box-like transverse density  
 428 profile of the source, the model predicts:

$$B_A \propto \exp[m_T(1/T_p - 1/T_A)] / (m_T R_{\parallel} (m_T) R_{\perp}^2 (m_T))^{A-1} \quad (7)$$

429 where  $R_{\perp}$  and  $R_{\parallel}$  are the femtoscopic radii of the source in the longitudinally co-  
 430 moving system [21],  $T_p$  and  $T_A$  are the transverse momentum slopes for proton  
 431 and nucleus A, respectively.

432 Figs. 13a and 13b show the  $B_2$  and  $B_3$  values as a function of the trans-  
 433 verse momentum measured in argon-nucleus interactions with centrality 0-40%.  
 434 The transverse momentum is scaled to the atomic number of the nuclear fragment  
 435 (deuteron, triton),  $p_T/A$ . The yields of protons ( $N_p$ ), deuterons ( $N_d$ ) and tritons  
 436 ( $N_t$ ) are measured in the same rapidity range, namely  $0.9 < y < 1.7$  ( $-0.18 <$   
 437  $y^* < 0.62$ ). Statistics of tritons are not sufficient to present  $B_3$  for Ar+C interac-  
 438 tions. It is found, that  $B_2$  and  $B_3$  are rising with  $p_T$  for all the measured targets, but  
 439 the dependence is close to linear rather than exponential. The  $B_2$  and  $B_3$  values  
 440 at low  $p_T$  are smaller for heavier targets compared to lighter targets.

Table 4: Coalescence parameters  $B_2(p_T = 0)$  and  $B_3(p_T = 0)$  extrapolated  
 to  $p_T = 0$  using an exponential fit to  $B_2(p_T)$  and  $B_3(p_T)$  and Coalescence radii  
 $R_{coal}^d(p_T = 0)$  and  $R_{coal}^t(p_T = 0)$  evaluated from the  $B_2(p_T = 0)$  and  $B_3(p_T = 0)$   
 values for deuterons and tritons produced in Ar+A interactions with centrality  
 0-40%.

	Ar+C	Ar+Al	Ar+Cu	Ar+Sn	Ar+Pb
$B_2(p_T = 0)/10^3, \text{ GeV}^2/c^3$	$5.5 \pm 1.9$	$1.7 \pm 0.5$	$1.8 \pm 0.4$	$1.2 \pm 0.4$	$1.1 \pm 0.2$
$B_3(p_T = 0)/10^6, \text{ GeV}^3/c^4$		$1.7 \pm 1.7$	$4.0 \pm 1.2$	$2.7 \pm 0.6$	$1.8 \pm 0.4$
$R_d(p_T = 0), \text{ fm}$	$2.1 \pm 0.3$	$3.1 \pm 0.3$	$3.0 \pm 0.2$	$3.5 \pm 0.4$	$3.6 \pm 0.2$
$R_t(p_T = 0), \text{ fm}$		$3.1 \pm 0.5$	$2.7 \pm 0.2$	$2.9 \pm 0.1$	$3.1 \pm 0.1$

441 In order to compare the present measurements of  $B_2$  and  $B_3$  with previously  
 442 obtained results, the  $B_2(p_T)$  and  $B_3(p_T)$  values given in Figs. 13a and 13b are  
 443 extrapolated down to  $p_T = 0$  using an exponential fit of the form  $B_A(p_T =$   
 444  $0) \exp(a \cdot p_T)$  as it is predicted by the coalescence model (see equation 7). To  
 445 evaluate the uncertainty of the parameter  $B_A(p_T = 0)$  the data errors are scaled  
 446 by a factor  $\sqrt{\chi^2/ndf}$  from the first iteration of the fit. The results of the extrap-  
 447 olation are given in Table 4.

448 The present results are compared in Fig.14a,b with the measurements of other  
 449 experiments [41,48–55]. The  $B_2$  and  $B_3$  results for Ar+A interactions with cen-

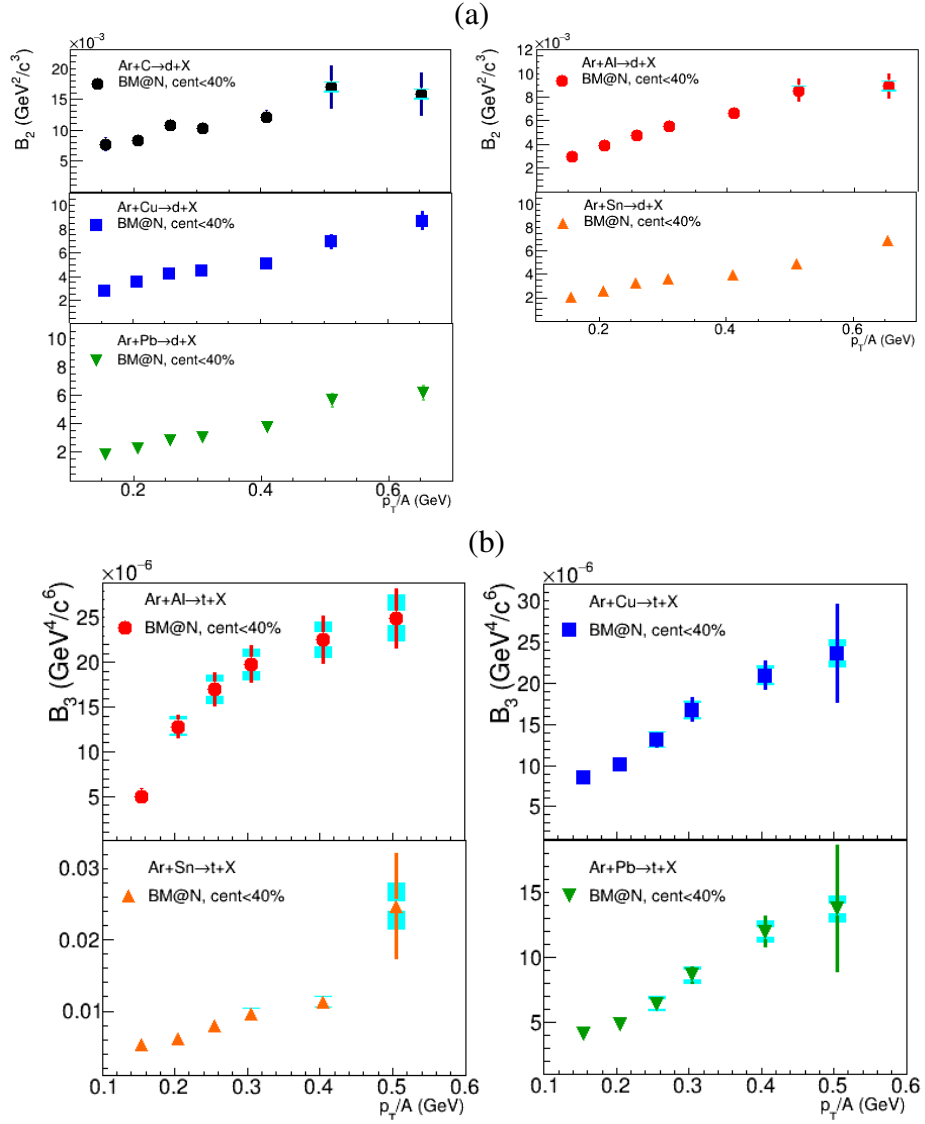


Figure 13: Coalescence parameter  $B_2$  for deuterons (a) and  $B_3$  for tritons (b) measured as a function of  $p_T/A$  in Ar+A collisions with centrality 0-40%.



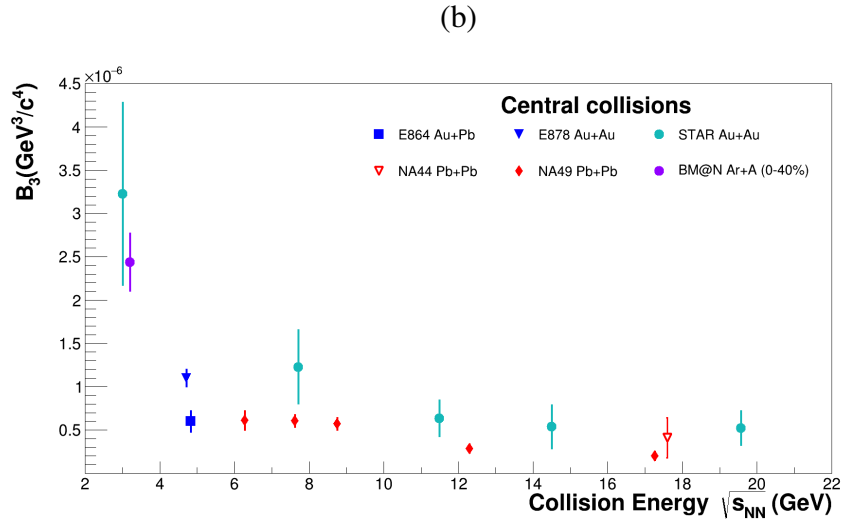
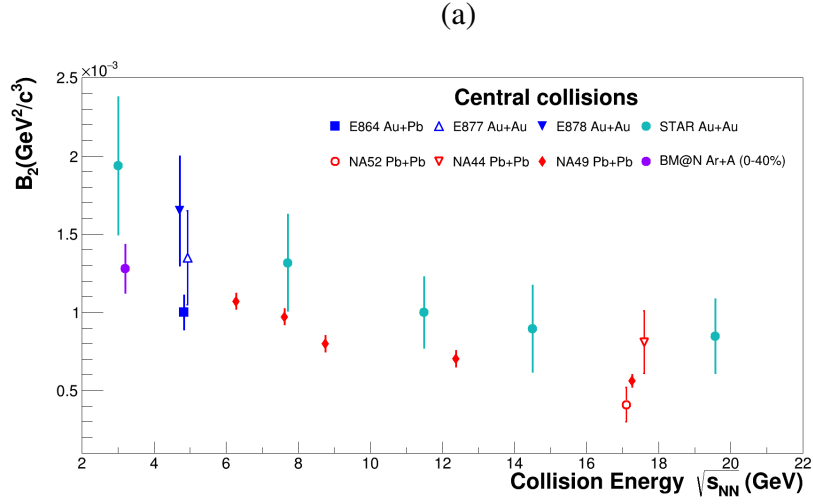


Figure 14: Coalescence parameters  $B_2(p_T = 0)$  (a) and  $B_3(p_T = 0)$  (b) for deuterons and tritons as a function of the centre-mass energy of nucleus-nucleus interactions. The BM@N result is the weighed average value calculated for Ar+Al,Cu,Sn,Pb interactions with centrality 0-40%.

450 trality 0-40% are consistent with the energy dependence of the  $B_2$  and  $B_3$  factors  
451 for central interactions of heavy nuclei. It can be seen, that the BM@N mea-  
452 surements follow the general trend of decreasing  $B_2$  and  $B_3$  values with rising  
453 collision energy. The  $B_2$  and  $B_3$  values are inversely related to the coalescence  
454 radius  $R_{coal}$  which is closely related to the femtoscopic radii of the source of pro-  
455 duced deuterons and tritons [21]. Using prescriptions in [48] based on [21], the  
456 coalescence source radius  $R_{coal} = \sqrt[3]{3/2R_{||}R_{\perp}^2}$  is calculated from the  $B_2(p_T = 0)$   
457 and  $B_3(p_T = 0)$  values of deuterons and tritons. In the calculations, the  $C_d$  and  
458  $C_t$  factors from [48] are scaled according to the mass of the colliding systems to  
459 account for the suppression related with the increased effective volume due to the  
460 finite deuteron and triton radii (see Eq. (4.12) in [21]). The resulting values are in  
461 the range of 0.55-0.61 and 0.48-0.53 for deuterons and tritons, respectively. The  
results for  $R_{coal}$  are given in Table 4.

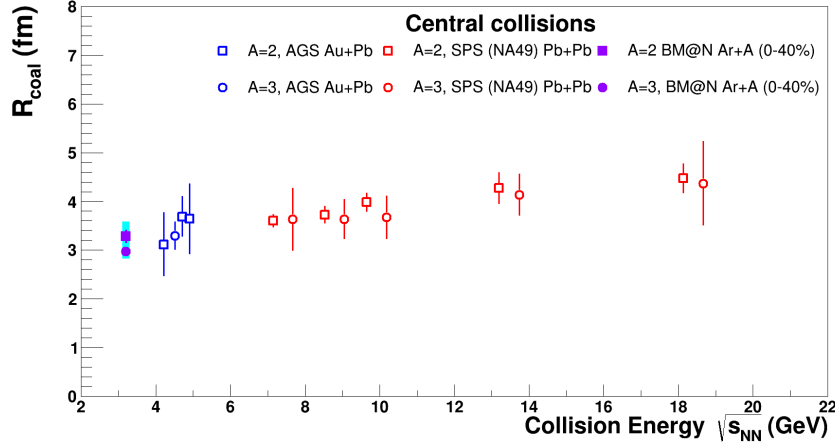


Figure 15: Coalescence radii  $R_{coal}$  for deuterons and tritons as a function of the centre-mass energy of nucleus-nucleus interactions. The BM@N result is the weighed average value calculated for Ar+Al,Cu,Sn,Pb interactions with centrality 0-40%.

462

463 The coalescence source radii for deuterons and tritons produced in Ar+Al,Cu,  
464 Sn,Pb interactions with centrality 0-40% are consistent with values of 3-3.5 fm ex-  
465 cept for deuterons produced in Ar+C interactions. The BM@N values for the co-  
466 alescence radii averaged for Ar+Al,Cu,Sn,Pb interactions are compared in Fig.15  
467 with results at higher energies as compiled in [41]. It is found that the BM@N re-  
468 sults are in agreement with the energy dependence of the coalescence source radii

469 of deuterons and tritons produced in heavy ion collisions. In general, the results  
 470 are in qualitative agreement with the naive expectation of decreasing homogene-  
 471 ity lengths and a smaller effective volume in collisions of smaller systems and at  
 472 lower energies.

## 473 **9 Baryon rapidity distributions, stopping and rapid-** 474 **ity loss in Ar+A**

The total baryon number in Ar+A collisions at NICA/BM@N energies is ba-  
 sically determined by the nucleons and the light nuclei ( $d, t, {}^3\text{He}$ ). According to  
 the results on the rapidity spectra of protons and light nuclei, presented in Sec-  
 tion 7, the number of nucleons bound in clusters contribute to the total number of  
 baryons up to about 15% and 25% in central Ar+C and Ar+Pb reactions, respec-  
 tively. To obtain the baryon rapidity distribution, we add up the baryon number  
 of the measured protons, deuterons and tritons in every rapidity bin. The obtained  
 distribution is then corrected for unmeasured baryons: neutrons, hyperons and  
 ${}^3\text{He}$  nuclei. Calculations with the PHQMD and UrQMD models indicate that for  
 all collision systems the  $n/p$ -ratio is of about 1.1 in the forward hemisphere vary-  
 ing slowly with rapidity and then increasing abruptly to  $\approx 1.22$  (the  $n/p$ -ratio in  
 the projectile Ar-nucleus) at the beam rapidity. We use these model predictions to  
 estimate the yield of neutrons  $n$ , furthermore, we assume that the  $t/{}^3\text{He}$  ratio is  
 equal to  $n/p$ . Hyperons contribute less than 2% to the total baryon number and are  
 thus neglected. The total number of baryons  $B$  in a rapidity bin is then calculated  
 as

$$B = p + n + 2.0 \cdot d + 5.7 \cdot t,$$

475 where the coefficient in front of  $t$  is  $5.7 = 3.0$  (for tritons) +  $3.0/1.1$  (for  ${}^3\text{He}$ ).

476 The resulting baryon rapidity distributions for Ar+Cu collisions are shown  
 477 in Fig. 16 as a function of the center-of-mass rapidity: the left panel shows the  
 478 results for 0-40% central collisions, and the right one is for peripheral collisions.  
 479 As one can see, more baryons are transported to midrapidity in the more central  
 480 collisions leading to a dramatic difference in the shapes of the  $dn/dy$  distributions.  
 481 To describe those shapes, we fitted the measurements to a  $3^{rd}$  order polynomial  
 482 in  $y^2$  (as suggested in ref. [56]), and the fit results are shown in Fig. 16 by solid  
 483 curves.

484 The average rapidity loss is calculated as

$$\langle \delta y \rangle = y_b - \langle y \rangle, \quad (8)$$

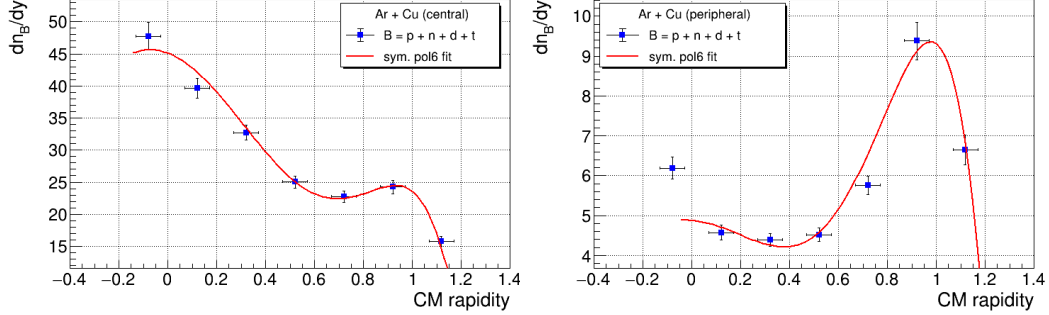


Figure 16: Left: Rapidity distribution of baryons in 0-40% central Ar+Cu collisions. The measurements are shown by solid dots, whereas the solid line is the results of a fit to a 3<sup>rd</sup> order polynomial in  $y^2$ . Right: same for peripheral Ar+Cu collisions.

Table 5: The average rapidity loss  $\langle \delta y \rangle$  in Ar+A reactions

	Ar+C	Ar+Al	Ar+Cu	Ar+Sn	Ar+Pb
0-40%	$0.47 \pm 0.03$	$0.54 \pm 0.03$	$0.60 \pm 0.03$	$0.62 \pm 0.04$	$0.64 \pm 0.04$
>40%	$0.39 \pm 0.03$	$0.42 \pm 0.03$	$0.47 \pm 0.03$	$0.53 \pm 0.04$	$0.55 \pm 0.04$

485 where  $y_b = 1.08$  is the rapidity of the projectile in the center-of-mass system, and

$$\langle y \rangle = \frac{\int_{y_0}^{y_b} y \frac{dn}{dy} dy}{\int_{y_0}^{y_b} \frac{dn}{dy} dy} \quad (9)$$

486 This equation refers to net-baryons, i.e. baryons minus antibaryons. At NICA  
 487 energies, however, the production of antibaryons is so small that the difference  
 488 between baryons and net-baryons is negligible. The low integration limit in Eq. 8  
 489 is the midrapidity ( $y_0 = 0$ ), but, the calculation result is correct only for a little  
 490 mixing of projectile and target participants. For the asymmetric Ar+A collisions,  
 491 considered here, we follow the suggestion from ref. [57] and define  $y_0$  such that  
 492 the area enclosed by the baryon  $dn/dy$  across the bounding values is equal to  
 493 the number of participating nucleons in the projectile  $N_p^{proj}$ . These numbers of  
 494 participants were determined by averaging the results of the UrQMD [58] and  
 495 DCM-SMM models. The  $y_0$  value varies from 0.12 for Ar+Pb to -0.3 for Ar+C  
 496 collisions.

497 The final  $\langle \delta y \rangle$  values for central and peripheral collisions are listed in Table 5.  
 498 A clear trend is observed:  $\langle \delta y \rangle$  increases with the target mass and with centrality.

499 This behavior is expected because the probability of multiple interactions in the  
 500 projectile-target overlap region is also rises with centrality and the target mass.

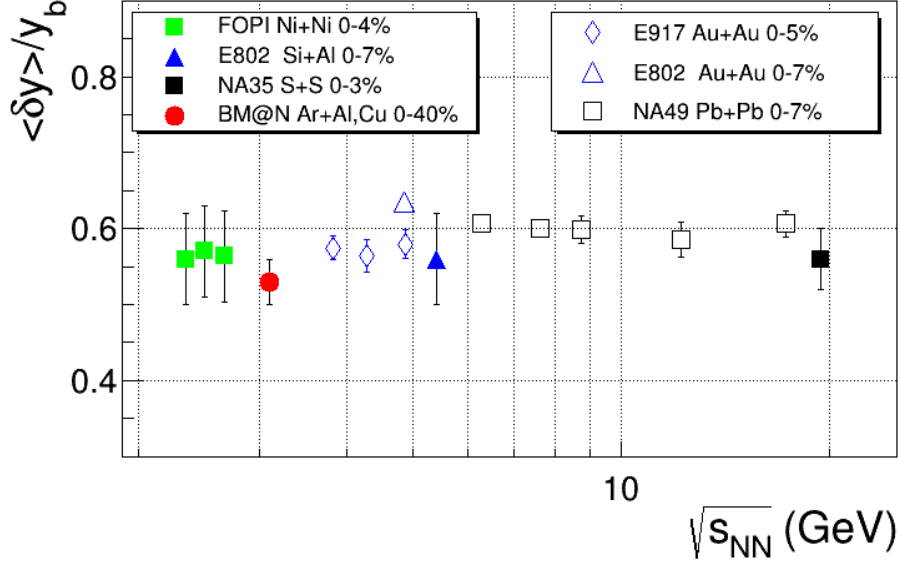


Figure 17: The excitation function of the scaled average rapidity loss  $\langle \delta y \rangle / y_b$  in ion-ion collisions. Medium-size colliding systems [57, 59, 60] are drawn by solid symbols, while heavy systems [57, 61, 62] are shown by open ones. Centrality intervals are indicated in the legends. The BM@N data point is the average of Ar+Al and Ar+Cu results.

501 Fig. 17 shows the energy dependence of the scaled average rapidity shift  
 502  $\langle \delta y \rangle / y_b$  in ion-ion collisions as a function of  $\sqrt{s_{NN}}$ . Results from medium-size  
 503 almost symmetric colliding systems from [57, 59, 60] are shown by solid symbols  
 504 and those from heavy colliding systems [57, 61, 62] are depicted by open symbols.  
 505 The corresponding centrality intervals are indicated in the legends. Here, the av-  
 506 erage of BM@N results obtained in Ar+Al and Ar+Cu reactions is shown. As one  
 507 can see, the scaled rapidity loss does not vary over a broad energy range.

## 508 10 Particle ratios

509 The rapidity and system size dependence of the deuteron-to-proton ratio  $R_{dp}$  in  
 510 Ar+A collisions at  $\sqrt{s_{NN}} = 3.1$  GeV is presented in Fig. 18, a)-e). As one can see,

511  $R_{dp}$  rises strongly from midrapidity to the beam rapidity in peripheral collisions.  
 512 The same trend is observed in central Ar+C collisions. In contrast, in central  
 513 collisions of argon nuclei with targets heavier than (or equal to) aluminum,  $R_{dp}$   
 514 indicates a plateau-like behavior near midrapidity followed by an increase toward  
 515 the beam rapidity region. The plateau region for  $R_{dp}$  increases gradually with the  
 516 target mass number covering almost all the measured rapidity range.

517 The midrapidity  $R_{dp}$  values from central and peripheral Ar+A collisions as  
 518 a function of the midrapidity baryon density  $dn_B/dy$  (obtained from the fits of  
 519 Fig. 16) is presented in Fig. 18, f). As one can see,  $R_{dp}$  increases steadily with  
 520 system size for small values of  $dn_B/dy$  and then levels off at higher values. For a  
 521 system in chemical equilibrium and if the size of the emitting source is larger than  
 522 the width of the deuteron wave function, the ratio of deuterons to protons can be  
 523 related to the average proton phase-space density at the freezeout  $\langle f_p \rangle$  as

$$\langle f_p \rangle = \frac{R_{pn}}{3} \frac{E_d \frac{d^3 N_d}{d^3 P}}{E_p \frac{d^3 N_p}{d^3 p}} \quad (10)$$

524 where  $R_{pn}$  is proton-to-neutron ratio,  $P = 2p$ , and the factor of 3 accounts for  
 525 the spins of the particles [13]. The  $\langle f_p \rangle$  value depends on the strength of nuclear  
 526 stopping in the reaction as well as on the outward flow effects. Thus, the observed  
 527 trend in Fig. 18, f) can be understood qualitatively as follows. On the one hand,  
 528 the proton phase-space density reached in the reaction zone decreases the more  
 529 peripheral the collision is, taking both the size of the deuteron cluster and the  
 530 participant volume into account. On the other hand, the baryon stopping (making  
 531 the fireball more dense) and the radial expansion (causing the baryons to occupy a  
 532 bigger volume and spread over a wider momentum range) can balance each other  
 533 in central collisions of argon nuclei with heavy target at NICA energies causing a  
 534 saturation of  $\langle f_p \rangle$ .

535 Figure 19 shows the evolution of the average proton's phase-space density as  
 536 a function of transverse momentum. Here, the particle yield ratios are obtained  
 537 in the rapidity range  $0.05 < y < 0.45$  and at three  $p_T/A$  values: 0.15, 0.3, and  
 538 0.45 GeV/c; the  $\langle f_p \rangle$  values are calculated according to Eq. 10. The values of the  
 539  $R_{pn}$  ratio in the chosen phase-space region were taken from the UrQMD model.  
 540 Some data points in the figure are displaced along the  $x$ -axis for the clarity. In  
 541 a thermal source at a low phase-space density ( $f \ll 1$ )  $\langle f_p \rangle$  follows a Boltzmann  
 542 distribution and decreases exponentially with  $p_T$  [63]. If, however, outward flow  
 543 is present in the system,  $f(p_T)$  may become flatter [64]. Taking into account the  
 544 results on the radial velocity and temperature presented in Table 3 (i.e. almost

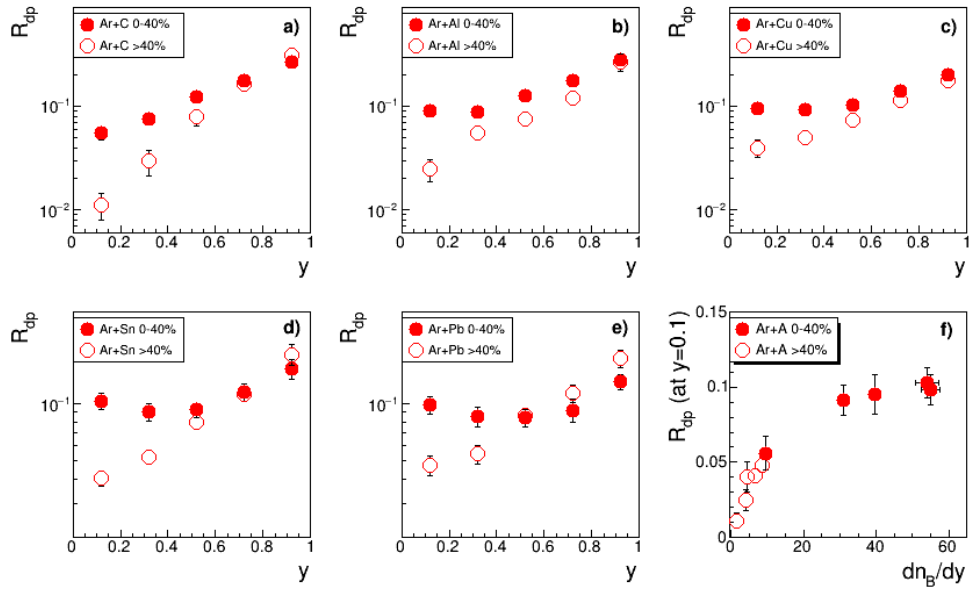


Figure 18:  $R_{dp}$  as a function of center-of-mass rapidity  $y$  in Ar+C (a), Ar+Al (b), Ar+Cu (c), Ar+Sn (d), and Ar+Pb (e) collisions. Central and peripheral collisions are shown by solid and open symbols, respectively. f): Midrapidity  $R_{dp}$  as a function of midrapidity baryon density  $dn_B/dy$  in Ar+A collisions.

545 no radial expansion in Ar+C and approximately the same values of  $T$  and  $\beta$  in  
 546 Ar+Al,Cu,Sn,Pb), one can conclude that the observed trend in Fig 19 is indeed  
 547 consistent with the expectations.

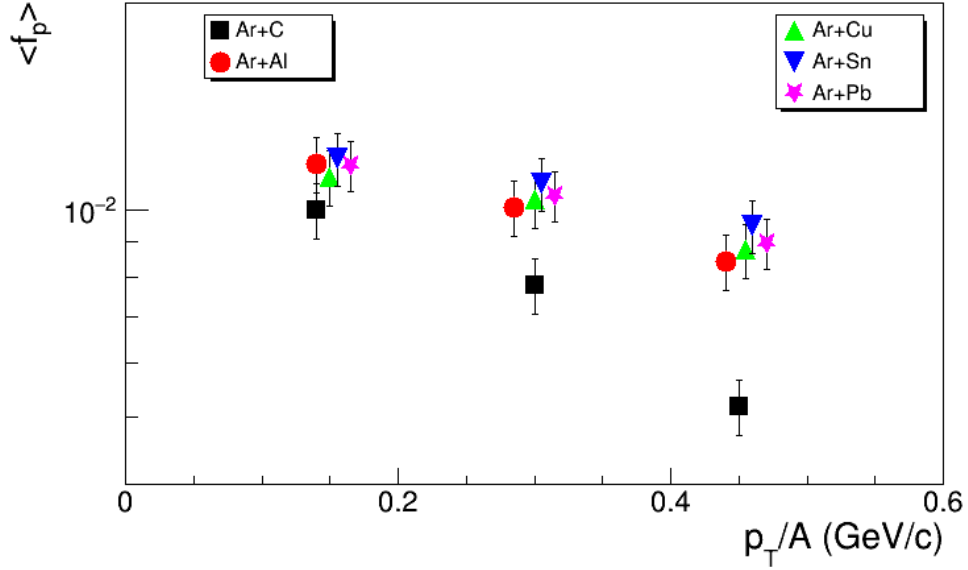


Figure 19: Average proton phase-space density for central Ar+A collisions as a function of  $p_T/A$  within the rapidity range  $0.05 < y < 0.45$ . The shown results are obtained at  $p_T = 0.15, 0.3, 0.45$  GeV/c, but displaced horizontally for the clarity.

548 It was identified long time ago that the nuclear cluster abundances and the  
 549 entropy value attained in the collisions are related. According to early investiga-  
 550 tions [65], in a mixture of nucleons and deuterons in thermal and chemical equilib-  
 551 rium the entropy per nucleon  $S_N/A$  can be deduced from the deuteron-to-proton  
 552 ratio  $R_{dp}$  as

$$\frac{S_N}{A} = 3.945 - \ln R_{dp} - \frac{1.25 R_{dp}}{1 + R_{dp}} \quad (11)$$

553 Furthermore, as the collision energy increases, the contribution of mesons  $S_\pi$   
 554 to the total entropy becomes important. Following [66], the entropy of pions per  
 555 nucleon can be estimated by

$$\frac{S_\pi}{A} = 4.1 \frac{N_\pi}{N_N}, \quad (12)$$

556 where  $N_N = N_p + N_n$  is the total number of nucleons.



557 We thus calculated the total entropy  $S/A$  near midrapidity as the sum of the  
 558 nucleon and pion entropy contributions according to Eq. 11 and Eq. 12. To es-  
 559 timate  $S_\pi$ , we used the recently published BM@N results on positively charged  
 560 pions [8], while the contribution of  $\pi^-$ ,  $\pi^0$ , and neutrons was obtained from the  
 561 UrQMD model. We found that the contribution of pions to the total entropy does  
 562 not exceed 25% in Ar+A collisions at NICA energies. Finally,  $S/A$  is found to be  
 563 10.6, 8.0, 8.0, 7.9, and 8.0 in central Ar+C, Ar+Al, Ar+Cu, Ar+Sn, and Ar+Pb,  
 564 respectively. The estimated uncertainty in  $S/A$  is about 15%. In Fig. 20 we present  
 565 the energy dependence of  $S/A$  in central heavy-ion collisions. This compila-  
 566 tion includes data from experiments that have published numerical values for the  
 567 midrapidity yields of charged pions, protons, and light nuclei [41, 59, 67–71]. In  
 568 this figure, we show the BM@N 'saturation'  $S/A$ -value of 8.0. As can be seen  
 from the figure, the total entropy increases steadily with collision energy.

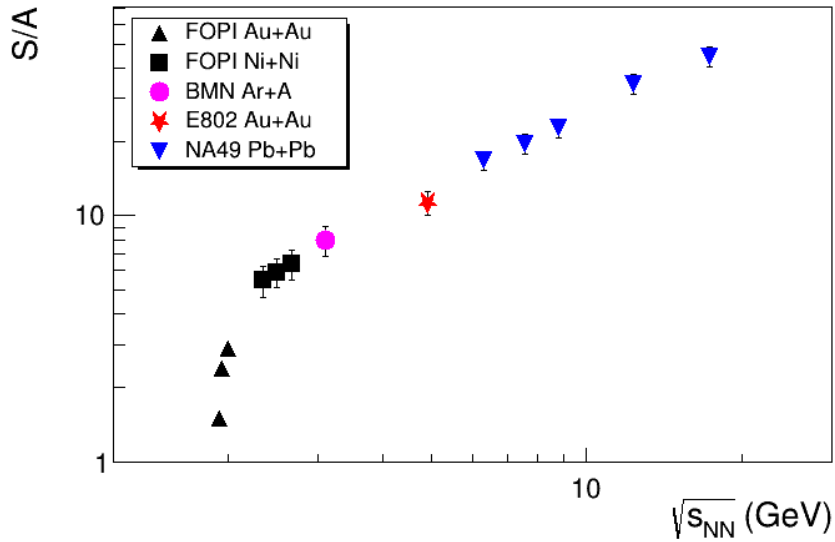


Figure 20: The excitation function of the entropy per baryon  $S/A$  from SIS/FOPI [59, 67], AGS/E802 [68], SPS/NA49 [41, 69–71] and NICA/BM@N (this study).

569 It has been established experimentally that the cluster production yields scaled  
 570 by the spin degeneracy factor  $(2J+1)$  decrease exponentially with the atomic mass  
 571 number  $A$  [41, 72]. As an example, Fig. 21 (left panel) presents  $dn/dy/(2J+1)$   
 572 at midrapidity for  $p, d, t$  as a function of  $A$  from 0-40% central Ar+Sn collisions.  
 573 Particle rapidity density values are extracted from the fits of Fig. 7. The  $A$ -  
 574

575 dependence of the yields was fitted to a form:

$$\frac{dn}{dy}(A) = \text{const}/p^{A-1}, \quad (13)$$

576 where the parameter  $p$  ('penalty factor') determines the penalty of adding one  
577 extra nucleon to the system.

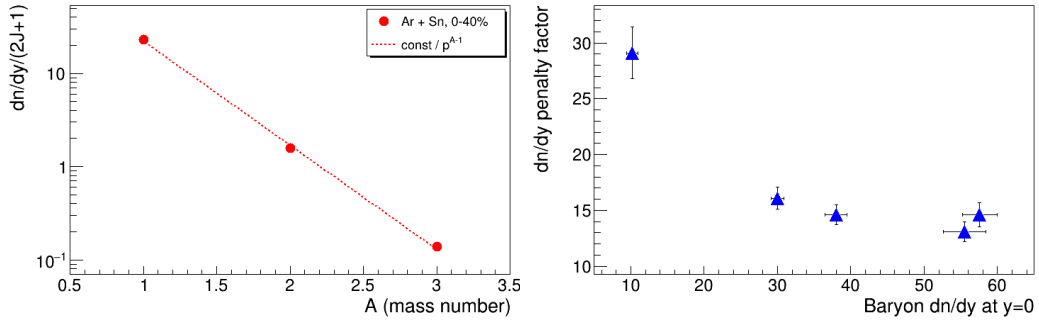


Figure 21: Left: Midrapidity  $dn/dy/(2J+1)$  for  $p, d, t$  from central Ar+Sn collisions. The dashed line is a fit to Eq. 13. Right: Penalty factor from central Ar+A collisions versus baryon rapidity density at  $y = 0$ .

578 The penalty factor is sensitive to the nucleon density attained in the reaction  
579 (the larger the density the smaller the penalty). The  $p$ -factors from central Ar+A  
580 collisions are listed in Table 6 and shown in Fig. 21 (right panel) as a function  
581 of the midrapidity baryon density. A clear trend is observed :  $p$  decreases for the  
582 small baryon densities reached in Ar+C and Ar+Al reactions and then saturates  
583 above  $dn/dy \approx 30$ .

584 In the framework of a statistical approach, the penalty factor is determined as:

$$p = e^{(m-\mu_B)/T}, \quad (14)$$

585 where  $\mu_B, T$ , and  $m$  being the baryochemical potential, freezeout temperature,  
586 and nucleon mass, respectively [15]. Equation 14 can be used to determine the  
587 source thermodynamic freeze-out parameters  $T$  and  $\mu_B$  as an alternative approach  
588 instead of the standard method based on the analysis of hadron abundances in the  
589 framework of a thermal statistical model (see [73] and references therein). As  
590 reported in ref. [74], the values of kinetic and chemical freeze-out temperatures are  
591 similar in heavy-ion collisions below  $\sqrt{s_{NN}} = 5$  GeV. Thus, we can use the value  
592 of  $T$  obtained in the analysis of transverse mass spectra of particles and listed

Table 6: Penalty factor  $p$ , temperature  $T$  (from Table 3), and baryochemical potential  $\mu_B$  in 0-40% central Ar+A collisions.

Reaction	$p$	$T$ (MeV)	$\mu_B$ (MeV)
Ar+C	$29.13 \pm 2.33$	$89.0 \pm 3.3$	$637.9 \pm 18.3$
Ar+Al	$16.07 \pm 0.97$	$90.9 \pm 8.2$	$685.3 \pm 22.9$
Ar+Cu	$14.55 \pm 0.74$	$79.5 \pm 5.4$	$725.1 \pm 16.6$
Ar+Sn	$13.09 \pm 0.72$	$76.3 \pm 9.1$	$742.5 \pm 23.5$
Ar+Pb	$14.63 \pm 0.83$	$80.4 \pm 10.2$	$722.3 \pm 27.2$

593 in Table 3 as an estimate for a 'universal' freeze-out temperature. Re-arranging  
 594 Eq. 14, one can write a formula for  $\mu_B$  as

$$\mu_B = m - T \ln p \quad (15)$$

595 The resulting  $(T, \mu_B)$  freeze-out parameters for central Ar+A collisions are  
 596 tabulated in Table 6 and shown in Fig. 22. The BM@N results from medium-  
 597 size Ar+A collisions follow the trend defined by world data and described by  
 598 the parameterization from ref. [73] (which is shown by the dashed line) with the  
 599 only exception of the Ar+C system that is probably too small to obtain a globally  
 600 equilibrated fireball.

601 Recently, the STAR experiment reported measurements of the compound yield  
 602 ratio  $R_{ptd} = N_p N_t / N_d^2$  of protons ( $N_p$ ) and tritons ( $N_t$ ) to deuterons ( $N_d$ ) [53].  
 603 Coalescence models predict [75] that a non-monotonic behaviour of the ratio as a  
 604 function of the system size or collision energy is a signature of the neutron density  
 605 fluctuations  $\Delta n$ :  $R_{ptd} \approx g(1 + \Delta n)$  with a color factor  $g \simeq 0.29$ . Following this  
 606 argument,  $R_{ptd}$  is a promising observable to search for the critical point and/or a  
 607 first-order phase transition in heavy-ion collisions [76]. In coalescence models,  
 608 the compound yield ratio should increase as the size of the system decreases.  
 609 Indeed, this effect is observed by the STAR experiment [54].

610 To evaluate the  $R_{ptd}$  ratio, mean values of the  $dN/dy$  distributions for protons,  
 611 deuterons and tritons are calculated in the rapidity range  $0.9 < y < 1.7$  ( $-0.18 <$   
 612  $y^* < 0.62$ ). The results are given in Table 7 for argon-nucleus interactions with  
 613 centrality 0-40%. No significant variation of the  $N_p N_t / N_d^2$  values is observed  
 614 with the various targets. Taking the differences as a systematic uncertainty, the  
 615 weighted average value of the compound ratio is estimated to be  $0.59 \pm 0.09$ , where  
 616 the uncertainty is the quadratic sum of the statistical and systematic uncertainties.  
 617 Within the uncertainties there is no dependence of the  $R_{ptd}$  ratio on rapidity in

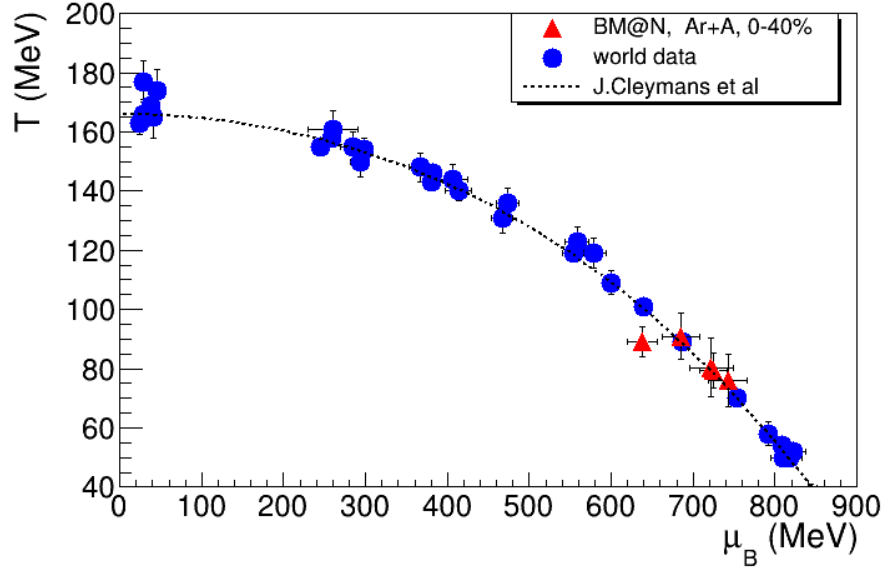


Figure 22: Freeze-out ( $T, \mu_B$ ) parameters for A+A collisions. BM@N results are from this study, world data and the parameterization for the freezeout line (dashed line) are from [73].

Table 7:  $N_p N_t / N_d^2$  values evaluated from the  $dN/dy$  data of protons, deuterons and tritons produced in the rapidity range  $-0.18 < y^* < 0.62$  in Ar+Ar interactions with centrality 0-40%.

	Ar+C	Ar+Al	Ar+Cu	Ar+Sn	Ar+Pb
$N_p N_t / N_d^2$	$0.53 \pm 0.10$	$0.55 \pm 0.09$	$0.69 \pm 0.11$	$0.60 \pm 0.07$	$0.59 \pm 0.06$

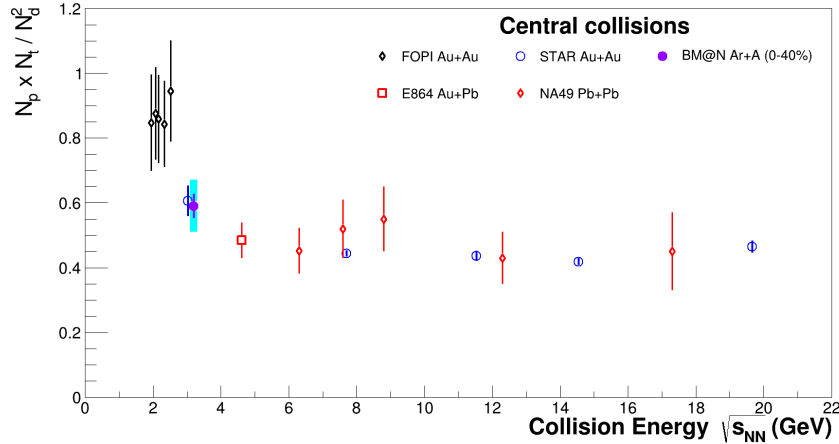


Figure 23: Compound yield ratio  $N_p \cdot N_t / N_d^2$  of protons ( $N_p$ ) and tritons ( $N_t$ ) to deuterons ( $N_d^2$ ) as a function of the centre-mass energy of nucleus-nucleus interactions. The BM@N result is the weighed average value calculated for Ar+Al,Cu,Sn,Pb interactions with centrality 0-40%.

618 the measured rapidity range. The BM@N value for  $R_{ptd}$  is compared in Fig. 23  
 619 with the measurements of other experiments. The BM@N result lays between the  
 620 values of 0.8-1.0 derived by the FOPI experiment [42] at lower energies and the  
 621 values of 0.4-0.5 obtained by the E864, STAR and NA49 measurements at higher  
 622 CM energies  $\sqrt{s}$  from 4.3 to 18 GeV [41, 49, 54, 77]. The BM@N value for  $R_{ptd}$   
 623 is consistent with the STAR measured at the fixed target at  $\sqrt{s}$  of 3 [55].

## 624 11 Summary

625 First physics results of the BM@N experiment are presented on the proton, deuteron  
 626 and triton yields and their ratios in argon-nucleus interactions at the beam kinetic  
 627 energy of 3.2 AGeV. The results are compared with the DCM-SMM and PHQMD  
 628 models and with the previously published results of other experiments.

629 The transverse mass  $m_T$  spectra are measured and the mean transverse kinetic  
 630 energy  $\langle m_T \rangle - m$  are presented for more central 0-40% events as functions of the  
 631 rapidity  $y$  and mass  $m$  of the nuclear fragment. The  $\langle m_T \rangle - m$  values are found to  
 632 depend linearly on the mass  $m$ . The source temperature at kinetic freeze-out and  
 633 the average radial velocity are extracted.

634 The rapidity spectra  $dN/dy$  of protons, deuterons and tritons are presented  
635 for the whole  $p_T$  range in two centrality ranges. The DCM-SMM and PHQMD  
636 models reproduce the shapes of the spectra, but underestimate the deuteron and  
637 triton yields by factors four and six, respectively.

638 The average rapidity loss  $\langle\delta y\rangle$  increases with the target mass and with the  
639 collision centrality. In contrast, the rapidity loss scaled to the beam rapidity  $\langle\delta y\rangle$   
640 in almost symmetric heavy-ion collisions does not vary over a broad energy range.

641 The ratio of deuterons to protons  $R_{dp}$  rises in peripheral collisions and levels  
642 off in central ones, possibly indicating a saturation of the nucleon phase-space  
643 density at freezeout. The entropy per baryon  $S/A$  was estimated to be  $S/A \approx 8$   
644 nicely fitting in the trend of the  $S/A$  energy dependence established from other  
645 experimental results.

646 The freezeout fireball parameters  $T$  obtained from the transverse mass spectra  
647 and the baryo-chemical potential  $\mu_B$  derived from a coalescence analysis were  
648 found to follow the trend defined by world data using a statistical analysis of  
649 particle abundances.

650 The deuteron to proton and triton to proton yield ratios are used to calculate  
651 the coalescence parameters  $B_2$  and  $B_3$  for deuterons and tritons. The coalescence  
652 radii of the deuteron and triton source are extracted from the  $B_2$  and  $B_3$  values  
653 extrapolated to  $p_T = 0$  and compared with results of other experiments. The  
654 compound yield ratio  $N_p N_t / N_d^2$  of protons and tritons to deuterons is evaluated  
655 and compared with other measurements at lower and higher energies. The results  
656 follow the general trend of the decreasing values of  $B_2$ ,  $B_3$  and  $N_p N_t / N_d^2$  ratio  
657 with increasing energy.

658 **Acknowledgments.** The BM@N Collaboration acknowledges the efforts of the  
659 staff of the accelerator division of the Laboratory of High Energy Physics at JINR  
660 that made this experiment possible. The BM@N Collaboration acknowledges  
661 support of the HybriLIT of JINR for the provided computational resources.

## 662 **References**

- 663 [1] B. Friman, W. Nörenberg, and V.D. Toneev, Eur. Phys. J. A 3 (1998).  
664 [2] J. Randrup and J. Cleymans, Phys. Rev. C 74 (2006) 047901.  
665 [3] Ch. Fuchs, Prog. Part. Nucl. Phys. 56 (2006) 1-103.

- 666 [4] NICA White Paper, Eur. Phys. J. A 52 (2016).
- 667 [5] BM@N Conceptual Design Report: [http://nica.jinr.ru/files/BM@N/BMN\\_](http://nica.jinr.ru/files/BM@N/BMN_)  
668 CDR.pdf
- 669 [6] M. Kapishin (for the BM@N Collaboration), Nucl. Phys. A 982 (2019) 967-  
670 970.
- 671 [7] M. Kapishin (for the BM@N Collaboration), SQM 2019 proceedings, 285  
672 Springer Proc. Phys. 250 (2020) 21-27.
- 673 [8] S.Afanasiev et al. (BM@N Collaboration), JHEP 07 (2023) 174.
- 674 [9] W. Busza and A. S. Goldhaber, Phys. Lett. 139B, 235 (1984).
- 675 [10] G.C. Rossi and G. Veneziano, Phys. Rep. 63 (1980) 153.
- 676 [11] A. Capella and B. Z. Kopeliovich, Phys. Lett. B 381, 325 (1996)
- 677 [12] D. Kharzeev, Phys. Lett. B 378, 238 (1996)
- 678 [13] M.Murray and B. Holzer, Phys Rev. C 63, 054901 (2000).
- 679 [14] A. Andronic, P. Braun-Munzinger, and J. Stachel, Phys. Lett. B 673, 142  
680 (2009).
- 681 [15] T.A. Armstrong et al (E864 Collaboration) Phys. Rev. Lett. 83, 5431 (1999).
- 682 [16] G. Bertsch and J. Cugnon, Phys. Rev. C 24, 2514 (1981).
- 683 [17] J. I. Kapusta, Phys. Rev. C 24, 2545 (1981).
- 684 [18] S.T. Butler and C.A. Pearson, Phys. Rev. 129, 836 (1963).
- 685 [19] A. Schwarzschild and C. Zupancic, Phys. Rev. 129, 854 (1963).
- 686 [20] S. Mrowczynski, Phys. Lett. B 277, 43 (1992).
- 687 [21] R. Scheibl and U. Heinz, Phys. Rev. C 59, 1585 (1999).
- 688 [22] N. Amelin, K. Gudima, and V. Toneev, Sov. J. Nucl. Phys. 51, 1093 (1990).
- 689 [23] M. Baznat, A. Botvina, G. Musulmanbekov, V. Toneev, V. Zhezher, Phys.  
690 Part. Nucl. Lett. 17 (2020) no. 3; arXiv: 1912.09277v.

- 691 [24] J.Aichelin, E. Bratkovskaya et al, Phys. Rev. C 101, 044905 (2020)
- 692 [25] BM@N project:  
693 [https://bmn.jinr.ru/detector/project/BMN\\_project.pdf](https://bmn.jinr.ru/detector/project/BMN_project.pdf)
- 694 [26] S. Afanasiev et al., arXiv:2312.17573 [hep-ex]
- 695 [27] D. Baranov et al., JINST 12 (2017) no. 06, C06041
- 696 [28] V. Babkin et al., Nucl. Instrum. Meth. A 824, P.490-492 (2016); V. Babkin  
697 et al., Proceedings of Science, 2014, Vol.213 (Proceedings of TIPP-2014),  
698 P.289.
- 699 [29] N. Kuzmin et al., Nucl. Instrum. Meth. A 916, P. 190-194 (2019).
- 700 [30] K. Alishina et al., Phys. Part. Nucl., 53 (2022) no. 2, 470-475.
- 701 [31] V. Akishina and I. Kisel, J. Phys.: Conf. Ser. 599, 012024 (2015), I. Kisel,  
702 Nucl. Instrum. Meth. A 566, 85 (2006).
- 703 [32] CERN Program Library, Long Writeup W5013, Geneva, CERN, 1993.
- 704 [33] <https://git.jinr.ru/nica/bmnroot>
- 705 [34] V.Plotnikov, L.Kovachev, A.Zinchenko, Phys. Part. Nuclei Lett. 20 (2023),  
706 1392–1402
- 707 [35] K.Kanaki, PhD Thesis, Technische Universität Dresden, 2007.
- 708 [36] H.Angelov et al., P1-80-473, JINR, Dubna.
- 709 [37] BM@N web-page:  
710 [https://bmn.jinr.ru/wp-content/uploads/2023/07/PiKpaper\\_TabRes\\_v3.pdf](https://bmn.jinr.ru/wp-content/uploads/2023/07/PiKpaper_TabRes_v3.pdf)
- 711 [38] STAR Collaboration: [nucl-ex] arXiv:2311.11020
- 712 [39] V.Vovchenko et al, Phys. Lett. B 809 (2020) 135746
- 713 [40] D.R. Tilley, H.R. Weller, G.M. Hale, Nucl. Phys. A 541 (1992) 1
- 714 [41] T.Anticic et al. (NA49 Collaboration) Phys. Rev. C 94, 044906 (2016)
- 715 [42] W.Reisdorf et al. (FOPI Collaboration) Nucl.Phys.A 848 (2010) 366-427



- 716 [43] M.A.Lisa et al. (EOS Collaboration) Phys.Rev.Lett.75 (1995) 2662
- 717 [44] L.Kumar (for the STAR Collaboration), Nucl. Phys. A 931, 1114 (2014)
- 718 [45] L.Adamczuk et al. (STAR Collaboration) Phys.Rev.C 96 (2017) 4, 044904
- 719 [46] A.Z.Mekjian, Phys. Rev. Lett. 38, 640 (1977); Phys. Rev. C 17, 1051 (1978);  
720 and Nucl. Phys. A 312, 491 (1978).
- 721 [47] J.I.Kapusta, Phys. Rev. C 21, 1301 (1980).
- 722 [48] I.G.Bearden et al. (NA44 Collaboration), Eur. Phys. J. C 23, 237–247 (2002).
- 723 [49] T.A.Armstrong et al. (E864 Collaboration), Phys. Rev. C 61, 064908 (2000),  
724 nucl-ex/0003009
- 725 [50] J.Barrette et al. (E877 Collaboration), Phys. Rev. C 61, 044906 (2000)
- 726 [51] M.J.Bennett et al. (E878 Collaboration), Phys. Rev. C 58, 1155 (1998).
- 727 [52] G.Ambrosini et al. (NA52 Collaboration), Phys. Lett. B 417, 202 (1998)
- 728 [53] M.Abdulhamid et al., STAR Collaboration, Phys.Rev.Lett. 130 (2023)  
729 202301
- 730 [54] D.Zhang (STAR Collaboration), Nucl. Phys. A 1005, 121825 (2021).
- 731 [55] arXiv:2311.11020 [nucl-ex]
- 732 [56] I.G. Bearden et al. (BRAHM Collaboration), Phys. Rev. Lett. 93, 102301,  
733 2004.
- 734 [57] F.Videbaek and Ole Hansen, Phys. Rev. C 52 (1995) 2684.
- 735 [58] S.A.Bass et al., Prog. Part. Nucl. Phys. 41 225 (1998).
- 736 [59] B.Hong et al (FOPI Collaboration), Phys. Rev. C 57 (1998) 244.
- 737 [60] J. Bachler et al (NA35 Collaboration), Phys. rev. Lett. 72 (1994) 1419.
- 738 [61] B.B.Back et al (E917 Collaboration), Phys. Rev. Lett. 86 (2001) 1970.
- 739 [62] C. Blume, for the NA49 Collaboration, J. Phys. G 34 (2007) S951.

- 740 [63] M. J. Murray, J. Phys. G 28, 2069 (2002).
- 741 [64] B. Tomasik and U. Heinz, Phys. Rev. C 65, 031902(R) (2002).
- 742 [65] L. P. Csernai and J. I. Kapusta, Phys. Rep. 131, 4 (1986) 223—318.
- 743 [66] S. Z. Belenkij and L. D. Landau, Nuovo Cimento, Supplement 3, 15 (1956).
- 744 [67] G. Poggi et al (FOPI Collaboration), Nucl. Phys. A 586, 755 (1995).
- 745 [68] L. Ahle et al (E802 Collaboration) Phys. Rev. C 60, 064901 (1999).
- 746 [69] T. Anticic et al (NA49 Collaboration), Phys. Rev. C 69, 024902 (2004).
- 747 [70] C. Alt et al (NA49 Collaboration), Phys. Rev. C 77, 024903 (2008).
- 748 [71] T. Anticic et al. (NA49 Collaboration) Phys.Rev.C 85 (2012) 044913
- 749 [72] T.A. Armstrong et al (E864 Collaboration) Phys. Rev. C 61,064908 (2000).
- 750 [73] J. Cleymans, H. Oeschler, K. Redlich, and S. Wheaton, Phys. Rev. C 73,  
751 034905 (2006).
- 752 [74] The STAR Collaboration, Phys. Rev. C 96,044904 (2017).
- 753 [75] K.-J.Sun et al., Phys.Lett.B 774 (2017) 103
- 754 [76] D.Oliinychenko, Nucl.Phys.A 1005 (2021) 121754
- 755 [77] M.Abdulhamid et al. (STAR Collaboration), Phys.Rev.Lett. 130 (2023)  
756 202301.